1 **Marine anoxia initiates giant sulfur-bacteria mat proliferation and associated changes in**

2 **benthic nitrogen, sulfur, and iron cycling in the Santa Barbara Basin, California**

3 **Borderland**

4 David J. Yousavich[1*], De'Marcus Robinson[2], Xuefeng Peng[3], Sebastian J. E. Krause[1,4], Frank

5 Wenzhoefer[5,6,7], Felix Janβen[5,6], Na Liu[8], Jonathan Tarn[8], Frank Kinnaman[8], David L.

6 Valentine[8], Tina Treude[1,2*]

8 [1]Department of Earth, Planetary, and Space Sciences, University of California Los Angeles, 595 Charles E.

9 Young Drive East, Los Angeles, CA 90095, USA

10 [2]Department of Atmospheric and Oceanic Sciences, University of California Los Angeles, Math Science

11 Building, 520 Portola Plaza, Los Angeles, CA 90095, USA

12 [3]School of Earth, Ocean, and Environment, University of South Carolina, 701 Sumter Street, EWS 617,

13 Columbia, SC 29208, USA

14 [4]Earth Research Institute, 6832 Ellison Hall, University of California Santa Barbara, Ca 93106-3060

15 [5]HGF-MPG Joint Research Group for Deep-Sea Ecology and Technology, Alfred-Wegener-Institute,

16 Helmholtz-Center for Polar and Marine Research, Am Handelshafen 12, 27570 Bremerhaven, Germany

17 [6]Max Planck Institute for Marine Microbiology, Celsiusstrasse 1, 28359 Bremen, Germany

18 [7]Department of Biology, DIAS, Nordcee and HADAL Centres, University of Southern Denmark, 5230 Odense

19 M, Denmark

20 [8]Department of Earth Science and Marine Science Institute, University of California, Santa Barbara, CA

21 93106, USA

23 **Correspondence:** David Yousavich (yousavdj@ucla.edu), Tina Treude (ttreude@g.ucla.edu)

24 **Abstract**

26 The Santa Barbara Basin naturally experiences transient deoxygenation due to its unique

27 geological setting in the Southern California Borderland and seasonal changes in ocean currents.

28 Long-term measurements of the basin showed that anoxic events and subsequent nitrate

29 exhaustion in the bottom waters have been occurring more frequently and lasting longer over the

30 past decade. One characteristic of the Santa Barbara Basin is the seasonal development of

31 extensive mats of benthic nitrate-reducing sulfur-oxidizing bacteria, which are found at the

32 sediment-water interface when the basin's bottom waters reach anoxia but still provide some

33 nitrate. To assess the mat's impact on the benthic and pelagic redox environment, we collected

34 biogeochemical sediment and benthic flux data in November 2019, after anoxia developed in the

35 deepest waters of the basin and dissolved nitrate was depleted (down to 9.9 µM). We found that

36 the presence of mats was associated with a shift from denitrification to dissimilatory nitrate

37 reduction to ammonium. The zone of sulfate reduction appeared near the sediment-water

38 interface in sediment hosting these ephemeral white mats, but that alone seems insufficient to

39 spur their growth. We found that a high sediment TOC content (>5%) and an exhaustion of iron

40 oxides in the surface sediment were additional prerequisites for mat proliferation. Our research

41 further suggests that cycles of deoxygenation and reoxygenation of the benthic environment

42 result in extremely high benthic fluxes of dissolved iron from the basin's sediment. This work

43 expands our understanding of nitrate-reducing sulfur-oxidizing mats and their role in sustaining

44 and potentially expanding marine anoxia.

Introduction

47 Naturally occurring low-oxygen waters in the ocean are commonly observed below the ocean's

48 mixed layer where respiration consumes oxygen faster than it is produced or ventilated. When

49 low oxygen conditions occur along the western continental shelf in regions susceptible to

50 upwelling events and/or undergoing eutrophication, organic matter remineralization can

51 frequently drive oxygen concentrations to hypoxic ($O_2 < 63$ μM) (Middelburg and Levin, 2009)

52 and/or anoxic levels ($O_2 < 3$ μM) (Fossing et al., 1995b; Canfield et al., 2010). These areas

53 usually referred to as Oxygen Minimum Zones (OMZs). In the water column of OMZs, nitrogen

54 transformation through canonical denitrification or dissimilatory nitrate reduction to ammonium

55 (DNRA) becomes the dominant organic matter remineralization mechanism (Ward et al., 2009).

56 OMZs within coastal basins that experience seasonal changes in upwelling can experience

57 anoxic and denitrifying conditions that extend to the benthic environment, especially when high

58 productivity (and associated organic matter export fluxes) coincide with seasonal patterns in

59 physical mixing. This fundamental change in the redox conditions at the sediment-water

60 interface encourages elevated rates of anaerobic microbial processes and promotes organic

61 matter preservation in the sediments (Middelburg and Levin, 2009; Treude, 2011). Persistent

62 anoxia in these coastal OMZ can lead to huge releases of sulfide (up to 13.7 mmol m^{-2} d^{-1}) and

63 ammonium (up to 21.2 mmol m^{-2} d^{-1}) into the water column (Sommer et al., 2016).

64

65 The Santa Barbara Basin (SBB) is a coastal basin in the California Borderland with an

66 approximate maximum depth of 600 m characterized by a seasonally anoxic water column

67 (Sverdrup and Allen, 1939; Sholkovitz and Gieskes, 1971). The transform boundary along the

68   California Borderland heavily affects the geomorphology of basins in this region; these basins

69   become twisted as the plates rub against each other and form a series of "bathtubs" blocked by

70   sills and seamounts off the coast of California. The SBB is bordered by the California coast in

71   the north, the Channel Islands in the south, the Santa Monica basin to the east, and the Arguello

72   Canyon to the west. A sill to the west of the basin at around 475 m depth (Fig. 1) prohibits most

73   water transfer between the Santa Lucia Slope and the deeper waters of the SBB (Sholkovitz and

74   Gieskes, 1971). The highly productive surface waters in the basin provide ample organic matter

75   to the basin's water column, encouraging strong remineralization processes below the euphotic

76   zone, which can induce anoxia below the sill depth, with typically less than 1 µmol O_2 L^{-1}

77   (Sholkovitz, 1973; Emery et al., 1962; Thunell, 1998; Emmer and Thunell, 2000). During

78   upwelling events (usually in Spring), oxygenated waters from the California Current spill over

79   the western sill and ventilate the SBB, increasing oxygen concentrations to approximately 20

80   µmol O_2 L^{-1} (Goericke et al., 2015). SBB water-column oxygen and nitrogen concentrations

81   have been evaluated through a longitudinal survey by the California Cooperative Oceanic

82   Fisheries Investigations (Calcofi) with data starting in the 1950's . The data collected by this

83   survey shows increasingly ubiquitous anoxia and denitrification in the basin with the SBB

84   becoming completely nitrate-depleted below the sill at least three times between 2012 and 2017

85   (https://calcof.iorg/data/).

86

87   These drastic changes in SBB oxygenation and seafloor redox conditions drive complex changes

88   in benthic biogeochemistry and microbiology, evidenced most clearly by the development of

89   thick, expansive mats of giant sulfur-oxidizing bacteria (GSOB) mats at the seafloor (Bernhard et

90   al., 2003; Prokopenko et al., 2006; Valentine et al., 2016; Kuwabara et al., 1999). A 2016 survey

91   of the basin seafloor identified a vast GSOB mat spread over 1.6 contiguous km, confined

92   between 487 and 523 km in the SBB depocenter where conditions were anoxic but not depleted

93   of NO_3^- (Valentine et al., 2016). Similar GSOB mats have been identified in several other

94   transiently deoxygenated OMZs including the Peruvian/Chilean coast (Sommer et al., 2016;

95   Schulz et al., 1996; Zopfi et al., 2001; Høgslund et al., 2009). These chemoautotrophic bacteria

96   (typically *Thioploca* and/or *Beggiatoa*) utilize sulfide as an electron donor and O_2 or NO_3^- as a

97   terminal electron acceptor (Jørgensen and Nelson, 2004). Some GSOB can hyperaccumulate

98   NO_3^- in cell vacuoles up to 500 mM (Fossing et al., 1995a) and use this NO_3^- reserve to oxidize

99   sulfide that diffuses from the underlying sediment to perform their metabolism. (Huettel et al.,

100   1996; Mußmann et al., 2003; Sayama, 2001).
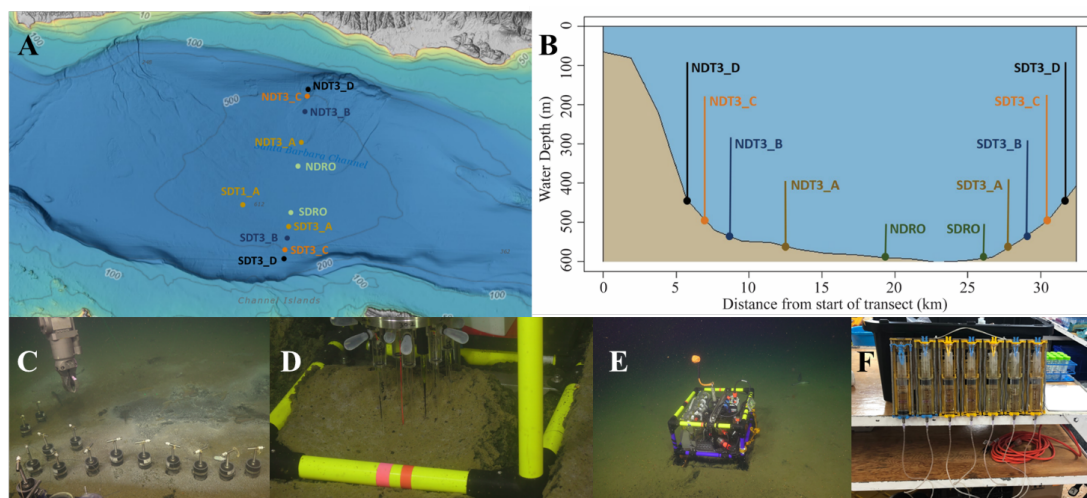
101
102
103   **Figure 1. Maps of sampling locations in the Santa Barbara Basin and photographs of**
104   **deployed equipment:** (A) bathymetric map of the Santa Barbara Basin with locations of all
105   sampled stations; (B) cross-section of the Santa Barbara Basin with locations of all sampled
106   station; (C) sediment push coring with ROV arm; (D) sediment microprofiler; (E) benthic flux
107   chamber; (F) closeup of a syringe system from a benthic flux chamber. The map in (A) was
108   generated using the Bathymetric Data Viewer provided by the National Centers for
109   Environmental Information.
110

111   These GSOB mats are ephemeral in the SBB, appearing to proliferate and potentially migrate

112   depending on bottom water oxidant concentrations (Kuwabara et al., 1999). The activity of

113   GSOB mats in turn contribute significantly to element cycling in the SBB with large effects on

114   biogeochemical conditions in the bottom water. Isotopic measurements of $^{15}N/^{14}N$ and $^{18}O/^{16}O$

115   from NO_3^- suggest that sedimentary organisms are responsible for approximately 75% of the total

116   NO_3^- uptake in the SBB (Sigman et al., 2003). Other studies found that GSOB mats inhibit the

117   diffusion of NO_3^- into sediments via hyper-accumulation in vacuoles thereby creating conditions

118   ideal for bacterial organoclastic sulfate reduction beneath them (Fossing et al., 1995b; Zopfi et

119   al., 2001). These studies suggest that GSOB mats in the SBB may be responsible for the majority

120   of NO_3^- consumption in the basin rather than water-column microbes. Additionally, GSOB mats

121   deplete NO_3^- via Dissimilatory Nitrate Reduction to Ammonium (DNRA) in the anoxic bottom

122   water of the Peruvian OMZ (Dale et al., 2016). By contrast, benthic microbial communities in

123   the hypoxic (42 µM) Mauritanian OMZ perform canonical denitrification instead (Dale et al.,

124   2014). The contrast between the Peruvian and Mauritanian OMZ suggests that anoxia triggers

125   the appearance of GSOB mats, and that DNRA is more prevalent where GSOB mats are present.

126

127   The rapid accumulation and consumption of NO_3^- by GSOB mats has ramifications for the redox

128   conditions in the sediment underneath. The depletion of NO_3^- and shallowing of the nitracline

129   could promote high rates of sulfate reduction in the sediment underneath the GSOB mat. In

130   return, the sulfate reduction zone exists close to the sediment-water interface, providing the

131   GSOB mat with readily accessible sulfide. If a metabolic feedback loop is then established

132   between sulfur-oxidizing bacteria at the sediment-water interface and sulfate-reducing bacteria in

133   the sediment, increased NO_3^- loss from the water column and spreading of sulfidic conditions in

134   SBB sediment is expected. With these mats being potentially crucial to nitrogen and sulfur

135   cycling in sediments underlying OMZ, their biogeochemical transformations and ergo effect

136   upon basin redox conditions are critically important to understanding element cycling in the

137   SBB. Such gained knowledge would have additional benefits for predicting biogeochemical

138   feedbacks to the projected expansion of oceanic oxygen deficiency, in the SBB and in OMZs

139   more general, as a result of global change (Stramma et al., 2008).

140

141   Utilizing in-situ technologies, sediment porewater extraction, solid phase analyses, and

142   radiotracer techniques, this study aims to answer the following overarching questions: (1) Which

143   environmental conditions initiate and sustain the proliferation of GSOB mats? (2) Which

144   biogeochemical transformations occur in the sediment underneath these mats? (3) What role do

145   the mats play in the increasingly prevalent anoxic and nitrate-depleted condition found in the

146   SBB?

2. Materials and Methods

2.1 Benthic sediment sampling and instrument deployment

Sediment samples were taken between 30 October and 11 November 2019 during an expedition

aboard the research vessel *(R/V) Atlantis* equipped with the remote operated vehicle (ROV)

Jason. Samples were taken at stations along a bimodal, north-south transect through the

depocenter of the SBB, as well as one station on a separate transect. Details of sampling stations

can be seen in Fig. 1A and 1B. Briefly, depocenter stations are labeled as NDRO and SDRO

(northern and southern depocenter radial origin, respectively). The remaining stations are named

for the cardinal direction (north vs. south) and the transect number (e.g., SDT1-A is on transect 1

while SDT3-A is on transect 3). As station depth decreases, the alpha suffix increases (e.g.,

NDT3-A is deeper than NDT3-B, etc.). ROV Jason conducted sediment push coring and

deployed automated benthic flux chambers (BFC) and microprofilers at each station. Station

depth, latitude, and longitude were automatically generated by the Jason data processor using

navigation data derived from the Doppler Velocity Log system and the ultrashort baseline

positioning system. Bottom water oxygen concentration was determined using an Aanderaa 4831

oxygen optode (Aanderaa Instruments, Bergen, Norway) installed on the ROV. Optical modems

(Luma 250LP, Hydromea, Renens, Switzerland) were used to transmit deployment settings and

initiate/terminate communications between ROV Jason and the BFC/microprofilers. Multiple

push cores (polycarbonate, 30.5 cm length, 6.35 cm inner diameter) per sampling station were

retrieved during ROV Jason deployments (Fig. 1C). These cores were inserted into the sediment

and retrieved using Jason's manipulator arm. Cores were then stored in a 6-core capacity basket

and transported to the surface using a free-ascending underwater elevator. Replicate cores from

each station were immediately transferred to a 6°C cold room (representing average in-situ

170   temperature) and subsampled for either solid phase analyses, porewater geochemistry, or

171   radiotracer experiments.

172

173   **2.2 Sediment Core Sub-Sampling**

174   For sediment porewater geochemistry analyses, two replicate ROV push cores that were

175   collected near each other were processed under a constant argon flow to protect redox-sensitive

176   species. Cores were sectioned in 1-cm increments up to 10 cm followed by 2-cm increments

177   below 10 cm. Note, sediments from the NDT3-B station were sliced in 2-cm increments.

178   Sediment subsections were transferred into argon-filled 50-mL conical centrifuge tubes.

179   Porewater was retrieved after sediment samples were centrifuged at 4255 x g for 20 minutes.

180   Solid phase cores were sectioned similar to porewater cores and sub-sampled for sediment

181   density and porosity and organic matter analyses. A cut-off plastic syringe was used to collect 6

182   mL of sediment into pre-weighed plastic vials (15 mL snap-cap vials) and stored in the dark at

183   4°C for sediment porosity and density analysis. Two-mL microcentrifuge tubes were filled with

184   sediment from each depth interval and stored at -30°C for sediment organic matter analyses. One

185   ROV push core per station was sub-sampled with a miniaturized push core (length 20 cm, inner

186   diameter 2.6 cm) and taken to the shipboard radioisotope van for radiotracer experiments (see

187   section 2.5).

188

189   **2.3 Sediment Porewater Geochemistry**

190   Geochemical analyses were performed to provide context for electron donors and acceptors of

191   benthic microbial metabolisms, sediment redox states, and organic matter degradation.

192   Concentrations of sulfide (Cline, 1969), NH_4^+, PO_4^{3-}, and Fe^{2+} (Grasshoff et al., 1999) were

193   determined shipboard with a Shimadzu UV-Spectrophotometer (UV-1800). Detection limits for

194   sulfide, NH_4^+, PO_4^{3-}, and Fe^{2+} were 1 µM. Subsamples (2 mL) for porewater NO_3^- and NO_2^-

195   concentrations were stored in 2-mL plastic vials with an O-ring, frozen shipboard at -30°C and

196   analyzed in the lab on the same spectrophotometer using the method following (García-Robledo

197   et al., 2014). The detection limit for NO_3^- and NO_2^- was 0.5 µM. Samples for porewater DIC

198   were preserved shipboard with 5 µL saturated HgCl in headspace free glass vials and stored at

199   4°C for later analysis following (Hall and Aller, 1992). DIC detection limit was 0.5 mM. Total

200   alkalinity was determined shipboard using direct titration of 500 µL of pore water with 0.01M

201   Titrisol® HCl (Pavlova et al., 2008). The analysis was calibrated using IAPSO seawater standard,

202   with a precision and detection limit of 0.05 meq L^{-1}. Subsamples (1 mL) for sulfate and

203   chlorinity were stored in 2-mL plastic vials with an o-ring, frozen shipboard at -30°C and later

204   measured in the lab using a Metrohm 761 ion chromatograph with a methodological detection

205   limit of 30 µM (Dale et al., 2015).

206

207   **2.4 Solid Phase Analyses**

208   Plastic vials for sediment porosity and density measurements were weighed prior to the

209   expedition. Samples collected in the vials were dried at 50°C for up to 96 hr until the dry weight

210   was stable. Sediment porosity was determined by calculating the difference between wet and dry

211   sediment weight divided by the volume of the wet sediment. Sediment density was determined

212   by dividing the wet sediment weight by its volume. Analyses for sediment total organic carbon

213   (TOC), total organic nitrogen (TON), and organic carbon isotope composition ($\delta^{13}C$) were

214   modified from (Harris et al., 2001). Briefly, samples were dried up to 48 hours at 50°C until the

215   dry weight was stable and then treated with direct addition of 1 mL of 6N HCl to dissolve

216   carbonate minerals. These samples were then washed in triplicate with 1-mL of ultrapure water

217   or until a neutral pH was re-established. Samples were centrifuged at 4255 x g for 20 minutes,

218   the supernatant was decanted, and vials were re-dried at 50°C. A subsample (approximately 10-

219   15 mg of sediment) was then packed into individual 8x5 mm pressed tin capsules and sent to the

220   University of California Davis Stable Isotope Facility for analysis using Elemental Analyzer –

221   Isotope Ratio Mass Spectrometry. TOC and TON were calculated based on the sample peak area

222   corrected against a reference material (alfalfa flour). Limit of quantification based on peak area

223   was 100 µg C with an uncertainty of ± 0.2 ‰ for $\delta^{13}C$.

224

225   **2.5 Sulfate Reduction**

226   To determine ex-situ microbial sulfate reduction rates, whole round sub-cores were injected with

227   10 µL carrier-free ^{35}S-Sulfate radiotracer (dissolved in water, 200 kBq, specific activity 37 TBq

228   mmol^{-1}) into pre-drilled, silicon-filled holes at 1-cm increments according to (Jørgensen, 1978).

229   These sub-cores were incubated at 6°C in the dark for 6-8 hours. Incubations were stopped by

230   slicing sediment cores in 1-cm increments into 50-mL centrifuge tubes filled with 20-mL zinc

231   acetate (20% w/w) and frozen at -20°C until analysis at the land-based laboratory. Triplicate

232   "killed" controls were produced using homogenized sediment from the same ROV push core.

233   Microbial activity in controls was terminated with zinc acetate (20 mL of 20% w/w) before the

234   addition of radiotracer and subsequent freezing. Lab-based analysis of sulfate reduction rates

235   were determined following the cold-chromium distillation procedure (Kallmeyer et al., 2004).

236   Sulfate reduction rates were calculated per volume of wet sediment (cm^3) following equation:

237

238     $$SRR = [SO_4] * P_{SED} * \frac{a_{TRIS}}{a_{TOT}} * \frac{1}{t} * 1.06 * 1000 \qquad \text{(EQ \# 1)}$$

239

240   Where SRR is sulfate reduction rate (nmol cm^{-3} d^{-1}); [SO$_4$] is porewater sulfate concentration;

241   Ps$_{ed}$ is sediment porosity; a$_{TRIS}$ is radioactivity of the total reducible inorganic sulfur (counts per

242   minute); a$_{TOT}$ is total radioactivity used in incubation (counts per minute); t is incubation time in

243   days; 1.06 is the correction factor for expected isotope fractionation; and 1000 is the factor to

244   convert from mmol to nmol.

245

246   **2.6 Benthic In-Situ Investigations**

247   Per station, one to three microprofiler (Fig. 1D) and three BFC (Fig. 1E) deployments were

248   carried out by the ROV Jason at the seafloor. Construction, deployment and operation of

249   automated microprofilers and BFCs followed those described in (Treude et al., 2009). The

250   mircoprofiler deployed in this study represents a modified, miniaturized version of the

251   instrument described in (Gundersen and Jørgensen, 1990) that was constructed specifically for

252   use by ROV. Microprofilers were outfitted with three O$_2$-microelectrodes (Glud et al., 2000),

253   two pH-microelectrodes (Revsbech and Jørgensen, 1986), two H$_2$S-microelectrodes

254   (Jeroschewsky et al., 1996), and one conductivity sensor to determine the position of the

255   sediment-water interface relative to the tips of the microelectrodes. Concentrations of oxygen

256   and sulfide, as well as pH were each calculated from microelectrode readings as an average per

257   site where replicates existed. Microprofiler frames (and benthic flux chamber frames) were

258   outfitted with syntactic foam to reduce the negative buoyancy of the instruments in water and

259   prevent them from sinking into the extremely soft sediments in the SBB.

260

261   The BFC consisted of a frame equipped with a cylindrical polycarbonate chamber (inner

262   diameter = 19 cm) with its lower portion sticking out of the frame. The upper side of the

263   chamber was closed by a lid containing a stirrer (Type K/MT 11, K.U.M., Kiel, Germany),

264   oxygen optodes (Type 4330, Aanderaa Data Instruments, Bergen Norway and Hydroflash,

265   Contros/Kongsberg Maritime, Kongsberg, Norway), a conductivity sensor (type 5860, Aanderaa

266   Data Instruments), and a valve. Prior to insertion into the sediments, the chambers were held

267   upside down by the ROV manipulating arms within approximately 10 m of the seafloor and

268   moved back and forth to make sure that water from shallower depth that may have been trapped

269   was replaced by bottom water. Chamber incubations lasted between 240 and 390 minutes. Each

270   BFC was outfitted with a custom-built syringe sampler containing seven syringes that were

271   connected by tubes to sampling ports in the upper wall of the chambers (Fig. 1F): one injection

272   syringe and six sampling syringes that were fired at regular time intervals over the time course of

273   the deployment. The injection syringe contained de-ionized water and the reduction in salinity in

274   the overlaying water after salinity readings stabilized (i.e., full mixing was achieved) 10-30 min

275   after injection was used to determine BFC volumes (Kononets et al., 2021). Samples obtained

276   from the overlaying water of the BFC were examined for the same geochemical constituents as

277   described above (section 2.4). Benthic fluxes of NO_3^-, NH_4^+, PO_4^{3-}, and Fe^{2+} were calculated as

278   follows:

279

280    $$J = \frac{\Delta c}{\Delta t} * \frac{V}{A}$$ (EQ # 2)

281

282   Where J is the diffusive flux in mmol m^{-2} d^{-1}, ΔC is the concentration change in mmol m^{-3}, Δt is

283   the time interval in d, V is the overlying water volume in m^3, and A is the surface area of the

284 sediment covered by the benthic flux chamber in m^2. Final diffusive flux in BFC was averaged

285 for stations of similar depth (e.g., we averaged calculated diffusive flux from NDT3-A and

286 SDT3-A and report as "A stations"). One chamber per site contained ^{15}N-NO$_3^-$ in the injection

287 syringe for in-situ nitrogen cycling experiments. Results are reported from two of these chambers

288 (SDRO and NDT3-D) and all ^{15}N-NO$_3^-$ chambers were excluded from benthic flux calculations

289 (see next section).

290

291 2.7.1 In Situ ^{15}N Incubations

292 Two hundred µmol of ^{15}N-labeled potassium nitrate (99% ^{15}N; Cambridge Isotopes) was injected

293 into the ^{15}N incubation chamber at each site to obtain a final concentration of ~50 – 100 µM ^{15}N-

294 labeled nitrate. Nitrate was amended at this level to prevent its depletion before the last sampling

295 time point (Valentine et al., 2016). Samples for δ^{15}N analysis were preserved by filling a pre-

296 vacuumed 12-ml exetainer vial with 0.1 ml 7M zinc chloride as a preservative. Another aliquot

297 (~12 ml) of seawater for ammonium isotope analysis (see section 2.7.2) was filtered through 0.2

298 µm syringe filters and stored frozen. Prior to analyzing the samples in 12-ml exetainer vials, 5

299 mL of sample was replaced with ultra-high purity helium to create a headspace. The

300 concentration and δ^{15}N of dissolved N$_2$ and N$_2$O was determined using a Sercon CryoPrep gas

301 concentration system interfaced to a Sercon 20-20 isotope-ratio mass spectrometer (IRMS) at the

302 University of California Davis Stable Isotope Facility.

303

304 2.7.2 Ammonium Isotope Analyses

305 The production of ^{15}NH$_4^+$ in seawater samples was measured using a method adapted from

306 (Zhang et al., 2007) and described previously by (Peng et al., 2016). In brief, NH$_4^+$ was first

307 oxidized to NO_2^- using hypobromite (BrO^-) and then reduced to N_2O using an acetic acid-azide

308 working solution (Zhang et al., 2007). The $\delta^{15}N$ of the produced N_2O was determined using an

309 Elementar Americas PrecisION continuous flow, multicollector, isotope-ratio mass spectrometer

310 coupled to an automated gas extraction system as described in (Charoenpong et al., 2014).

311 Calibration and correction were performed as described in (Bourbonnais et al., 2017). The

312 measurement precision was ±0.2 ‰ for $\delta^{15}N$. Depending on the in-situ ammonium

313 concentration, the detection limit for total NH_4^+ production rates ranged between 0.006 and

314 0.0685 mmol m^{-2} d^{-1}.

315

3. Results

3.1 Bottom water conditions

Oxygen and nitrate concentrations in the bottom water, i.e., in the water surrounding the ROV

during its operations at the seafloor and in the benthic flux chambers at T_0, respectively, along

the transects can be seen in Table 1. O_2 concentration decreased with basin depth, with average

concentrations of 9 and 10 µM at the shallowest stations (NDT3-D and SDT3-D, respectively)

and concentrations below detection (<3 µM) at the deepest stations (NDRO and SDRO), which

were confirmed to represent anoxia by different methods (see discussion section 4.1). Bottom

water solute concentrations (as defined by the average time 0 concentration in BFC at each site)

can be seen in Suppl. Figs. 1-4. Bottom water NO_3^- concentrations decreased with station depth;

NO_3^- was 27 and 28 µM at NDT3-D and SDT3-D, respectively, and decreased to 19 and 10 µM

at NDRO and SDRO, respectively. Bottom water NO_2^- concentrations were below detection at

all stations. Bottom water NH_4^+ concentrations were 9 µM at NDRO and 13 µM at SDRO and

below detection in shallower stations. Bottom water PO_4^{3-} concentrations showed similar trends

to NH_4^+, with an average concentration of 1 and 2 µM at NDT3-D and SDT3-D stations,

respectively, and 5 and 7 µM at NDRO and SDRO stations, respectively. Finally, Fe^{2+} was 2 and

5 µM at the NDRO and SDRO stations, respectively. Bottom water Fe^{2+} was below detection at

all shallower stations.

3.2 Sediment characteristics
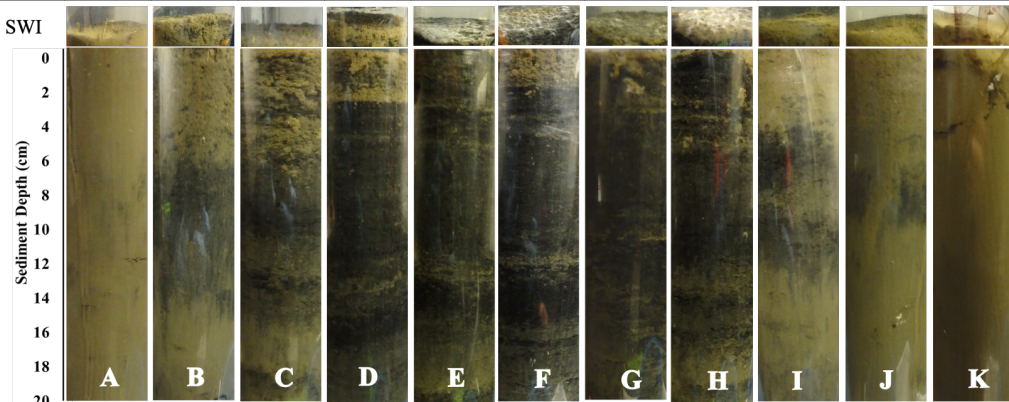
Photographs of sediment cores with a depth scale are shown below Table 1. Sediment colors

were classified according to (Hossain et al., 2014). Cores from the shallowest (D) stations were

uniformly reddish in color with small pockets of black. The sediment color changed with station

339 depth, transitioning from a reddish color in the shallowest stations to predominantly black with

340 reddish laminations at the depocenter stations. The band of black sediment appeared at approx. 8

341 cm sediment depth in the C-station cores and became progressively more ubiquitous with station

342 depth. Sediment cores from shallower stations (D and C stations) contained signs of bioturbation

343 and, in some cases, contained visible macrofauna, such as polychaetas and mollusks. Deeper in

344

345 **Table 1.** Station details and photos of representative ROV push cores taken at each station. Mat presence (Y =
346 yes, N = no) was determined visually. Station water depth and oxygen concentration were determined by sensors
347 attached to ROV Jason. Anoxia was confirmed by additional methods (see discussion section 4.1). Latitude and
348 longitude were determined by triangulation between the ROV and the ship. Bottom water nitrate concentration
349 was derived from an average of benthic flux chamber nitrate measurements at time 0 for each station (chambers
350 with no calculatable flux and ^{15}N-nitrate addition excluded). Note, benthic flux chambers were not deployed at
351 SDT1-A. Photographs show the sediment-water interface (SWI; top part) and each sediment core in full length
352 (lower part).
353

Parameter	NDT3-D	NDT3-C	NDT3-B	NDT3-A	NDRO	SDRO	SDT1-A	SDT3-A	SDT3-B	SDT3-C	SDT3-D
Mat Present	N	N	N	Y	Y	Y	Y	Y	N	N	N
Depth (m)	447	498	537	572	580	586	573	571	536	494	447
Latitude (°)	34.363	34.353	34.333	34.292	34.262	34.201	34.212	34.184	34.168	34.152	34.142
Longitude (°)	-120.015	-120.016	-120.019	-120.026	-120.031	-120.044	-120.116	-120.047	-120.053	-120.050	-120.052
Oxygen (µM)	8.7	5.2	12.2	9.2	0.0	0.0	0.0	0.0	1.8	3.1	9.6
Nitrate (µM)	27.3	26.0	11.5	24.4	18.5	9.9		20.4	20.6	16.3	28.0

354
355

356

357 the basin (A and depocenter stations) no signs of bioturbation were detected, and the sediment-

358 water interface was colonized by patches of white GSOB mats. Spherical cells (given the

359 moniker 'ghost balls') were found mixed amongst giant sulfur bacteria filaments within the top

360 0-1 cm of sediment at NDRO (Suppl. Fig. 5). These unknown species had similar morphological

361 characteristics to the species *Thiomargarita namibiensis* (Schulz et al., 1999; Schulz and Schulz,

362 2005) containing a translucent cell with sulfur granules giving them a ghostly white appearance.

363 A small sample of cells were measured, with a diameter that ranged from 48.0 – 99.6 µm (n = 8),

364 amounting to an average biovolume of 2.5 x 10^5 µm^3, compared to *T. namibiensis* with a cell

365 diameter up to 700 µm (Schulz et al., 1999).

366
367 **Table 2.** Sediment solid phase data: porosity, density, total organic carbon (TOC), total organic nitrogen (TON),
368 C:N ratio, and δ13C. All data were averaged for the top 0-19 cm sediment, except NDT3-C (17 cm), NDT3-A
369 (11 cm) and SDRO (7 cm), where the core length was shorter. Integrated sulfate reduction rates (iSRR) were
370 integrated over 0-14 cm sediment depth. No sulfate reduction rates are available for NDT3-B, SDT3-A, and
371 SDT3-B; rates were not integrated for SDRO due to missing surface samples.
372

Parameter	NDT3-D	NDT3-C	NDT3-B	NDT3-A	NDRO	SDRO	SDT1-A	SDT3-A	SDT3-B	SDT3-C	SDT3-D
Porosity	0.79 ± 0.03	0.81 ± 0.04	0.86 ± 0.04	0.88 ± 0.03	0.88 ± 0.04	0.87 ± 0.03	0.88 ± 0.03	0.86 ± 0.04	0.85 ± 0.04	0.82 ± 0.04	0.78 ± 0.04
Density (g cm^{-3})	1.21 ± 0.07	1.16 ± 0.08	1.06 ± 0.08	1.05 ± 0.04	1.06 ± 0.03	1.04 ± 0.03	1.11 ± 0.23	1.05 ± 0.05	1.12 ± 0.06	1.22 ± 0.05	1.22 ± 0.03
TOC (%)	3.67 ± 0.00	3.89 ± 0.01	4.65 ± 0.01	5.23 ± 0.01	5.05 ± 0.01	5.34 ± 0.01	5.23 ± 0.01	5.83 ± 0.01	5.05 ± 0.01	4.53 ± 0.01	4.13 ± 0.00
TON (%)	0.41 ± 0.00	0.45 ± 0.00	0.55 ± 0.00	0.62 ± 0.00	0.62 ± 0.00	0.66 ± 0.00	0.61 ± 0.00	0.71 ± 0.00	0.61 ± 0.00	0.52 ± 0.00	0.49 ± 0.00
C:N Ratio	8.9 ± 0.2	8.7 ± 0.5	8.5 ± 0.5	8.2 ± 0.2	8.2 ± 0.4	8.0 ± 0.2	8.6 ± 0.8	8.3 ± 0.6	8.3 ± 0.3	8.7 ± 0.3	8.5 ± 0.2
δ^{13}C (‰)	-22.4 ± 0.3	-22.4 ± 0.4	-22.2 ± 0.4	-22.1 ± 0.2	-22.1 ± 0.2	-22.0 ± 0.3	-21.3 ± 0.7	-22.1 ± 0.4	-22.0 ± 0.2	-21.9 ± 0.2	-22.0 ± 0.1
iSRR (mmol m^{-2} d^{-2})	2.9	3.8		2.7	4.1		2.9			1.7	1.9

373
374
375
376 B station cores contained sporadic filaments slightly deeper in the sediment (approx.. 2-4 cm

377 sediment depth). Depocenter and A-station sediment was laminated throughout the entire core

378 length, B-station sediment showed some lamination below the first 4 cm, but sediment from

379 shallower stations had little (C station) to no signs of lamination (D station). Sediment solid

380 phase parameters (averaged over the entire sediment core depth) can be seen in Table 2. Average

381 sediment porosity increased with basin depth (e.g., from 0.79 at NDT3-D to 0.88 at NDRO).

382 TOC and TON increased slightly with station depth (from 3.67% TOC and 0.41 TON at NDT3-

383 D to 5.34% and 0.66% TON at SDRO) while the C/N ratio and the δ^{13}C isotopic signature of

384   organic carbon remained relatively constant (8.0 – 8.7 and 21.3 – 22.4 ‰, respectively) over all

385   stations.

386

387   **3.3 Sediment porewater geochemistry**

388   Geochemical parameters of sediment porewater are shown in Fig. 2 (northern stations) and 3

389   (southern stations). Total alkalinity (Figs. 2 A-E & 3 A-F) increased steadily with sediment depth

390   at all stations starting with, on average, 2.4 mM in the core supernatant reaching a maximum at

391   the respective deepest sediment sample (20 cm). Total alkalinity also increased with basin depth;

392   cores in the depocenter exhibited higher total alkalinity (max. 9.6 mM at NDRO) than D-stations

393   (max. 3.4 mM at NDT3-D). Porewater DIC (Figs. 2 A-E & 3 A-F) showed patterns very similar

394   to total alkalinity, indicating that total alkalinity was dominated by the carbonate system.

395   Porewater DIC was, on average, 2.2 mM in the core supernatant and reached maximum

396   concentrations at the deepest sediment depth (20 cm) at most stations. Porewater DIC also

397   increased with basin depth; depocenter sediment had higher DIC concentrations (max. 8.3 mM at

398   NDRO) than D-station (max. 2.8 mM at NDT3-D).

399

400   Porewater PO_4^{3-} profiles (Figs. 2 A-E & 3 A-F) were markedly different between the depocenter

401   and shallower C and D stations. PO_4^{3-} concentration increased by approx. one order of magnitude

402   between the core supernatant and the 0-1 cm section at most stations (e.g., 7 and 48 µM at

403   NDRO, respectively). Porewater PO_4^{3-} concentrations in the depocenter and A stations generally

404   increased with sediment depth but several profiles (NDT3-C, NDT3-A, SDRO, SDT1-A)

405   remained unchanged or decreased deeper in the sediment (starting at approx. 10 cm). The

406   profiles in C and D stations showed a peak in PO_4^{3-} concentrations near the sediment-water

407 interface, particularly in the northern basin. Below 2 cm, PO_4^{3-} decreased with sediment depth,

408 but sometimes showed a second small peak deeper in the sediment (12-14 cm at NDT3-D and

409 10-12 cm at SDT3-D).

410

411 Porewater NH_4^+ concentrations (Figs 2 & 3 A-E) showed trends often similar to alkalinity and

412 DIC; NH_4^+ concentrations increased downcore and were higher at depocenter than at D stations

413 (e.g., 370 and 91 μM at 20 cm for SDRO and SDT3-D, respectively). NH_4^+ concentration

414 increased by approx. one order of magnitude between the core supernatant and the 0-1 cm

415 section at most stations (e.g., 16 μM and 139 μM at NDRO, respectively). Supernatant NH_4^+ was

416 below detection at D and C stations (and SDT3-B) and above 10 μM at the deeper A (except

417 SDT1-A) and depocenter stations. NO_2^- and NO_3^- were at or near zero concentration below 2 cm

418 at every station. NO_3^- concentration decreased substantially in the transition from core

419 supernatant to the 0-1 cm section at most stations (e.g., 24 μM and 0 μM at NDT3-D,

420 respectively). Sediment cores from SDRO and NDT3-A stations exhibited strong peaks in NO_3^-

421 (376 and 81 μM, respectively) and NO_2^- (37 and 5 μM, respectively) in the top 1 cm.

422

423 Porewater Fe^{2+} concentrations (Figs. 2 F-J & 3 G-L) were several orders of magnitude higher at

424 shallow D stations (max. 722 and 395 μM at NDT3-D and SDT3-D, respectively) compared to

425 depocenter stations (max. 13 and 51 μM at NDRO and SDRO, respectively). Fe^{2+} concentration

426 increased by approx. one order of magnitude between the core supernatant and the 0-1 cm

427 section at all stations (e.g., 16 μM and 139 μM at NDRO, respectively). Concentrations reached

428 a max. at 0-2 cm and declined sharply with depth in depocenter and A-station sediment.

429 Northern basin sediment was similar, but the decline in Fe^{2+} below 0-2 cm was less pronounced.

430

431   Max. porewater sulfide concentrations (Figs. 2 F-J & 3 G-L) were several orders of magnitude

432   lower at shallow D stations (5 and 4 µM at NDT3-D and SDT3-D, respectively) compared to A

433   stations (350 and 148 µM at NDT3-A and SDT1-A, respectively). Unlike Fe^{2+}, peaks in sulfide

434   concentration occurred deeper in the sediment (e.g., below 5 cm depth at A stations). Porewater

435   sulfate concentrations (Figs. 2 K-O & 3 M-R) decreased slightly with depth, but never reached

436   values below 20 mM at any station.

437

438   **3.4 In-situ microprofiling**

439   Microprofiler O_2 and sulfide measurements are shown in Fig. 4. Oxygen was rapidly consumed

440   within the first 0-1 cm of sediment at every station where O_2 was detected in the bottom water

441   (i.e., at all stations except NDRO, SDRO, and SDT3-A, which were anoxic). Sulfide

442   concentrations from microsensors showed similar trends to spectrophotometric measurements,

443   albeit with different absolute values (e.g., 196 and 808 µM sulfide at the 7 cm depth at NDT3-A

444   using the cline method and microprofilers, respectively). Sulfide was below detection of the

445   microprofilers in shallower stations (B, C, and D), all of which lacked GSOB mats. The A and

446   depocenter stations had high sulfide concentrations (>1,000 µM) in the sediment underlying

447   GSOB mats, which rapidly decreased towards zero near the sediment-water interface.

448   Microprofiler pH (Fig. 4) was near 7.5 in the bottom water at all stations, and slowly decreased
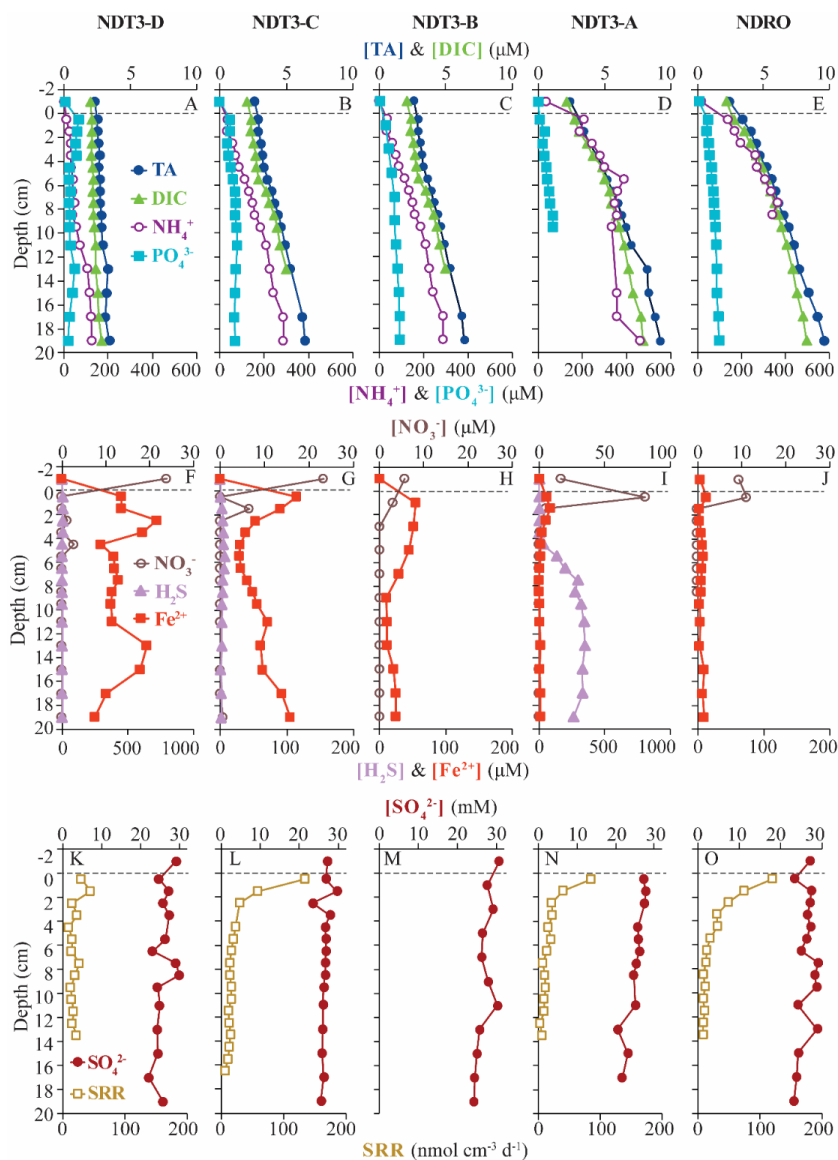
Figure 2. Biogeochemical data from ROV sediment push cores collected at stations on the northern transect (NDT3) and in the northern depocenter (NDRO): total alkalinity (TA), dissolved inorganic carbon (DIC), ammonium (NH_4^+), phosphate (PO_4^{3-}) in the first row; nitrate (NO_3^-), total sulfide (sulfide), and iron (II) (Fe^{2+}) in the second row; sulfate (SO_4^{2-}) and bacterial sulfate reduction rate (SRR) in the third row. Data analyzed from sediment core supernatant are plotted at -1 cm sediment depth; the dotted line connotes the sediment-water interface. Note the change in scale on the primary x-axis in panel I and the change in scale of the secondary x-axis in panels F and I. No sulfide and SRR data are available for NDT3-B. For station details see Fig. 1 and Table 1.
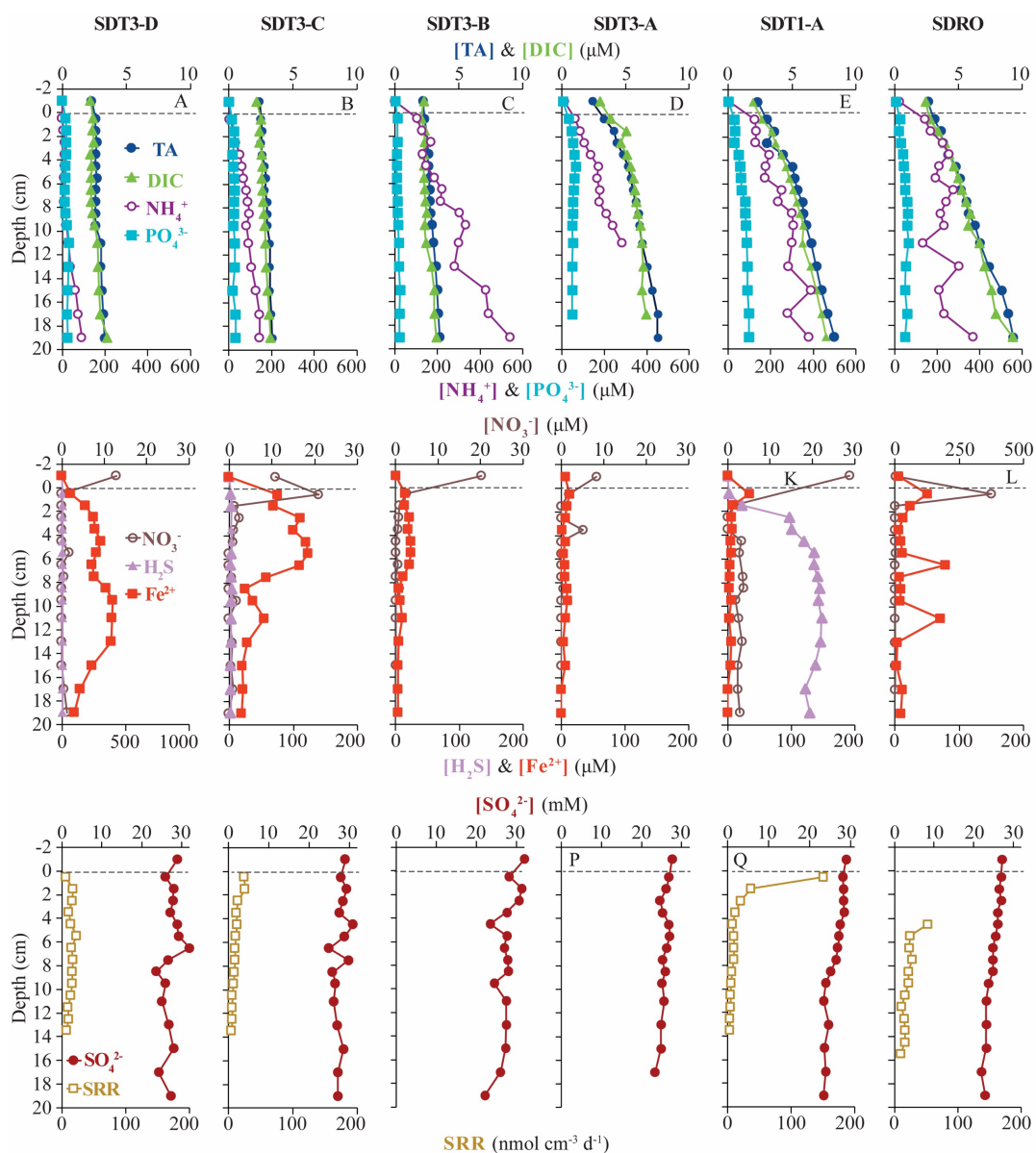
Figure 3. Biogeochemical data from ROV sediment push cores collected at stations on the two southern transects (SDT1 and SDT3) and the southern depocenter (SDRO): total alkalinity (TA), dissolved inorganic carbon (DIC), ammonium (NH_4^+), phosphate (PO_4^{3-}) in the first row; nitrate (NO_3^-), total sulfide (sulfide), and iron (II) (Fe^{2+}) in the second row; sulfate (SO_4^{2-}) and bacterial sulfate reduction rate (SRR) in the third row. Data analyzed from sediment core supernatant are plotted at -1 cm sediment depth; the dotted line connotes the sediment-water interface. Note the change in scale on the primary x-axis in panel L and the change in scale of the secondary x-axis in panel G. No sulfide and SRR data are available for SDT3-B and -A; at SDRO, the top 0-4 cm of sulfate reduction data are not available. For station details see Fig. 1 and Table 1.

468   to near 7.0 within the top 20 cm of sediment at most stations. At NDT3-C and SDT3-D, pH

469   exhibited no discernable trend over depth with values remaining around pH 7.5.

470
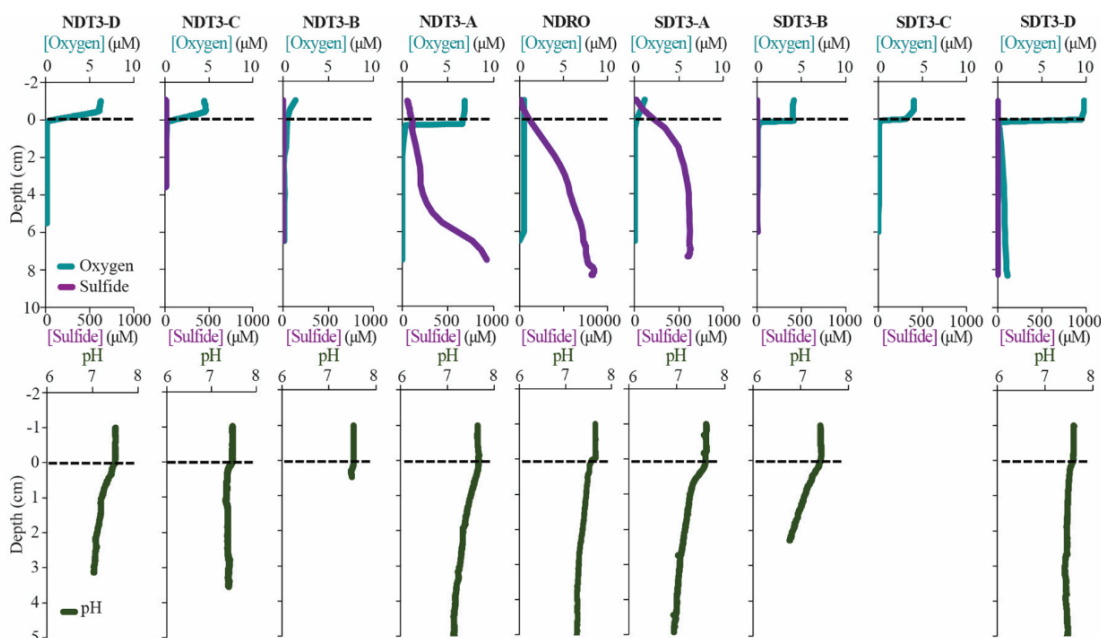
471
472
473   **Figure 4.** In-situ sediment microprofiler results for all stations (except SDT1-A): oxygen (O_2) and total sulfide
474   (sulfide) concentration in the first row; pH profiles in the second row. Note the change in scale on the secondary
475   x-axis for NDRO sulfide. Values determined in the overlying water are plotted at negative sediment depths; the
476   dotted line connotes the sediment-water interface.
477

478   **3.5 In-situ fluxes of benthic solutes**

479   NO_3^-, NH_4^+, PO_4^{3-}, and Fe^{2+} flux measured in the BFC revealed different patterns of uptake and

480   release from the sediment throughout the basin (Fig. 5 and Suppl. Figs. 1-4). BFC O_2

481   concentrations were compromised by O_2 release from the chamber's polycarbonate walls, which

482   prevented an accurate calculation of O_2 fluxes from sensor data. NO_3^- was consumed at all

483   stations as indicated by a negative flux (i.e., a flux into the sediment). On the contrary, benthic

484   release (i.e., a flux out of the sediment) was observed for all other analyzed solutes (NH_4^+, PO_4^{3-},

485   and Fe^{2+}), with the lowest fluxes in the shallow D and C-stations and highest fluxes in the

486   depocenter. Ammonium fluxes were the highest of all the determined solutes and showed the

487   largest difference between deep and shallow stations, with a flux of 1.6 mmol m^{-2} d^{-1} at NDT3-C

488   (there were no measurable NH_4^+ fluxes in D-station chambers) and reaching 11.1 ± 3.1 mmol m^{-2}

489   d^{-1} (n = 3) at the two depocenter stations. The depocenter ammonium flux far-outpaced the

490   concomitant flux of nitrate into depocenter sediments (-3.2 ± 0.7 mmol m^{-2} d^{-1}, n = 3). Iron and

491   phosphate fluxes were similar at depocenter stations (4.1 ± 0.7, n = 3, and 3.2 ± 0.7, n = 3, mmol

492   m^{-2} d^{-1}, respectively) but there was no discernable trend between the two solutes at shallower

493   stations. Results from BFCs injected with ^{15}N-NO_3^- at the SDRO and NDT3-D station are shown

494   in Fig. 6. The rates of denitrification, anammox, and N_2O production were higher at SDRO

495   compared to NDT3-D. $^{15}NH_4^+$ production (DNRA) was one order of magnitude higher at the

496   SDRO station (2.674 mmol m^{-2} d^{-1}) compared to the NDT3-D station (0.140 mmol m^{-2} d^{-1}).

497   DNRA accounted for a much higher percentage of NO_3^- reduction at SDRO (54.1%) than NDT3-

498   D (13.3%).

499

500   **3.6 Sulfate reduction rates**

501   Vertical profiles of bacterial sulfate reduction as determined by the radioisotope technique

502   differed throughout the basin (Figs. 2 & 3). Peaks in sulfate reduction (120.2, 151.0, 85.3 nmol

503   cm^{-3} d^{-1}) were seen in the top 0-1 cm of sediment at stations with a visible GSOB mat on the

504   surface (NDRO, SDT1-A, NDT3-A, respectively). Sediments at most shallower basin depths

505   (SDT3-C, NDT3-D, and SDT3-D) exhibited peaks slightly deeper in the sediment and of lower

506   magnitude (25.5, 44.5, 22.5 nmol cm^{-3} d^{-1} respectively). NDT3-C had no visible GSOB mats

507   present but also exhibited a peak (133.7 nmol cm^{-3} d^{-1}) in sulfate reduction at 0-1 cm depth.
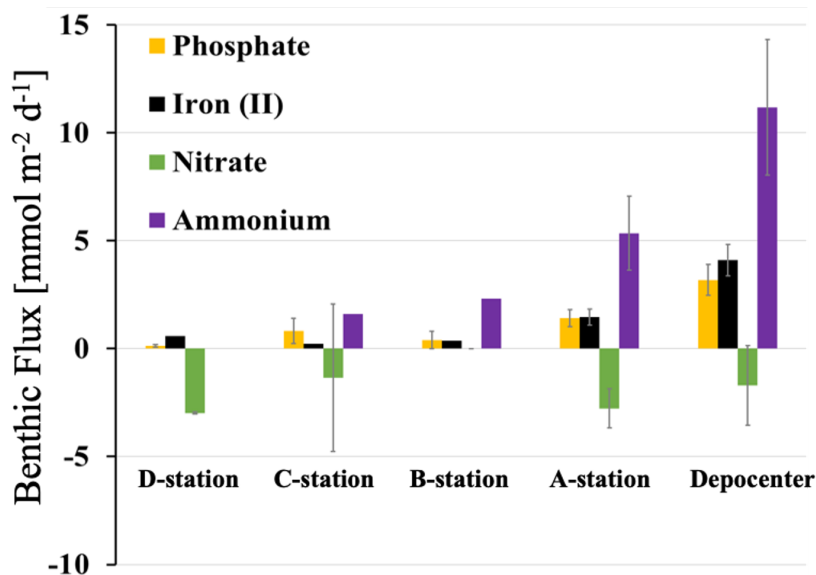
Figure 5. Benthic fluxes of solutes (positive flux = release from the seafloor; negative flux = uptake by the seafloor) determined with in-situ benthic flux chambers. Rates were averaged for stations of same depth from the northern and southern transect and the depocenter (NDRO and SDRO). Error bars represent standard errors.
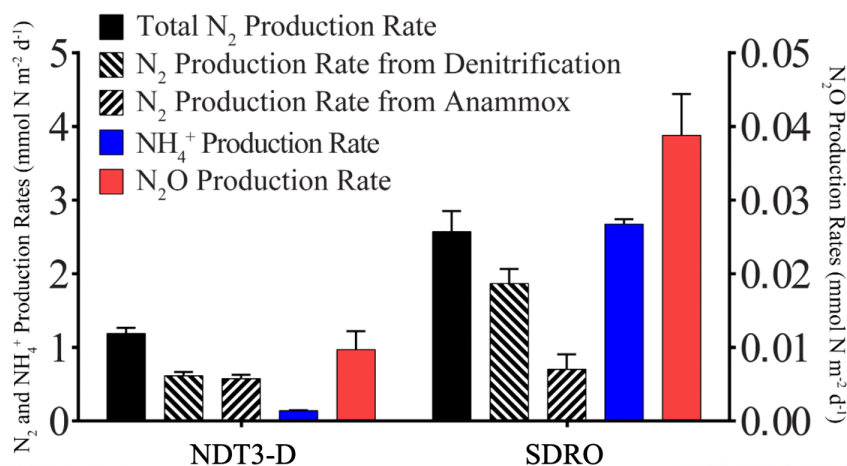
Figure 6. Areal rates of total N_2 production, denitrification, anammox, NH_4^+ production (DNRA), and N_2O production

Sulfate reduction rates at depocenter and A stations decreased sharply below 0-1 cm sediment

depth (up to an order of magnitude decrease at NDRO and SDT1-A), while remaining low and

521   steady over depth in C and D station sediment. Integrated sulfate reduction rate (0-14 cm depth)

522   at NDRO (4.1 mmol m^{-2} d^{-1}) was noticeably higher than most other stations with the exception of

523   NDT3-C (3.8 mmol m^{-2} d^{-1}) (Table 2). NDT3-D and NDT3-C exhibited higher integrated rates

524   (2.9 and 3.8 mmol m^{-2} d^{-1}) than their southern station counterparts SDT3-D and SDT3-C (1.9 and

525   1.7 mmol m^{-2} d^{-1}).

4. Discussion

4.1 Giant sulfur-oxidizing bacterial mats proliferated in response to deoxygenation in the Santa Barbara Basin

The SBB is an ideal environment to study the effect of transient deoxygenation on benthic biogeochemistry. In November 2019, the SBB was undergoing a transition from oxygenated to anoxic conditions (Qin et al., 2022). When the AT42-19 cruise occurred, most of the bottom water in the basin was hypoxic (B, C, and D stations), except for the depositional center and the A stations. Importantly, separate O_2 measurements from the ROV sensor (Table 1), microprofiler (Fig. 4), and Winkler titration from CTD/rosette casts (Qin et al., 2022) indicated full anoxia in the bottom water at these deeper stations. Notably, bottom water conditions revealed a slight asymmetry between the basin transects (Fig. 1); bottom water along the northern transect had generally more O_2 and NO_3^- than the southern transect (e.g., 9 µM at NDT3-A and 0 µM at SDT3-A). This asymmetry indicated differences in the circulation and/or microbial communities between the northern and southern portions of the basin. Whether this asymmetry is a permanent feature of the basin or symptomatic of the specific conditions in November 2019 is unclear; previous studies in the SBB have been restricted to the depocenter or one side of the basin (Sholkovitz, 1973; Reimers et al., 1996; Kuwabara et al., 1999). Regardless of bottom water oxidant concentration, the energetically most powerful terminal electron acceptors (O_2 and NO_3^-) disappeared in a very narrow zone below the sediment-water interface (Fig. 4 and Figs. 2 and 3, respectively), consistent with their expected rapid consumption by the benthic microbial community.

548   The sediment-water interface represents the front-line in a battle between microbes for powerful

549   electron acceptors. In the present study, benthic GSOB mats were primarily limited to the anoxic

550   depocenter of the SBB. Similarly, such mats were replete in the core of the anoxic Peruvian

551   OMZ (Levin et al., 2002; Sommer et al., 2016; Mosch et al., 2012), but absent from the seafloor

552   below the hypoxic, i.e., slightly oxygenated, Mauritanian OMZ (Schroller-Lomnitz et al., 2019).

553   GSOB mats in November 2019 were observed deeper in the basin than in October 2013

554   (Valentine et al., 2016) but in a similar location to June 1988 (Reimers et al., 1996) and April

555   1997 (Kuwabara et al., 1999). During the 2013 sampling, dense GSOB mats were confined to

556   depths between approx. 500-570 m (equivalent to the B stations from this expedition),

557   corresponding with anoxic conditions in the bottom water. This habitat was sandwiched between

558   an anoxic, anitric (i.e., nitrate-free) deep and a hypoxic, nitrigenated (i.e., nitrate-rich) shallower

559   water layer. The difference in depth distribution between the 2013 and 2019 expedition provides

560   evidence that GSOB mats in the SBB are ephemeral and proliferate where the bottom water is

561   anoxic but not anitric.

562

563   As our study represents only a snapshot of an oxygen- and nitrate-driven mat dynamic, we can

564   only speculate how areas of the basin that did not contain GSOB mats in November 2019 fit into

565   this dynamic. For example, mat-forming sulfur bacteria found slightly deeper in the sediment at

566   B stations (see section 3.2) could be progenitors to surface sediment colonization of thick GSOB

567   mats, as it has been recorded in other transiently deoxygenated environments (Jørgensen, 1977).

568   Alternatively, these subsurface colonies could also be remnants of a former surface GSOB mat

569   that retreated under changing redox conditions. Oxygenated conditions in the water preceding

570   the 2019 expedition would, in this context, mean the mats migrated following a previous anoxic

571   event (Qin et al., 2022). If deoxygenation persisted in the SBB after the AT42-19 cruise, then

572   anitria (i.e., anitric conditions - similar to anoxia) would likely follow in the deepest basin water.

573   These conditions would be similar to those seen during the 2013 expedition by D. Valentine and

574   co-workers (Valentine et al., 2016), where GSOB mats formed a contiguous "donut ring" at

575   shallower basin depths.

576

577   4.2 Shift from benthic denitrification to dissimilatory nitrate reduction to ammonium in

578   response to complete deoxygenation in the Santa Barbara Basin

579

580   Benthic release and uptake of nitrogen species by SBB sediment appeared to be affected by the

581   presence of GSOB mats. While benthic nitrate consumption was evident at all stations based on

582   porewater and in-situ flux measurements, NH_4^+ release from the sediment into the water column

583   increased with station depth (Fig. 5). This trend is supported by the porewater profiles of NH_4^+,

584   which tend to increase in steepness with station depth (Figs. 2 & 3). Incubations with ^{15}N-NO_3^-

585   revealed that N_2 production via denitrification and anammox accounted for 86% of NO_3^- removal

586   in the shallow basin (NDT3-D, Fig. 6). Conversely 54% of NO_3^- removal at the depositional

587   center (SDRO) occurred via DNRA (X. Peng et al., to be submitted to this special issue). This

588   data suggests a transition from denitrification-dominated sediment in the oxygenated basin to an

589   increasing influence of DNRA on N-cycling in the deeper, anoxic basin. Placed in the context of

590   other OMZs, nitrate consumption in the shallow SBB sediment (below hypoxic water) was

591   similar to Mauritanian shelf sediments (Dale et al., 2014), while nitrate consumption in the

592   sediment of the deeper SBB (below anoxic water) was similar to anoxic Baltic Sea basins (Dale

593   et al., 2011) and the core Peruvian OMZ (Sommer et al., 2016).

594

595   Declining nitrate concentrations may be as important as anoxia itself to GSOB mat proliferation.

596   High ratios of electron donor (organic matter or sulfide) to electron acceptor (nitrate) encourage

597   DNRA over denitrification (Marchant et al., 2014). In these nitrate-deficient areas in the ocean,

598   DNRA linked to anaerobic ammonium oxidation (anammox) can be more thermodynamically

599   favorable and thus organisms that participate in this consortium could have a competitive

600   advantage over other denitrifying organisms (Jensen et al., 2011). NO_2^- was at or near-zero

601   concentrations in the sediment porewater of all stations, except in the 0-1 cm depth interval of

602   two stations (SDRO and NDT3-A) featuring GSOB mats (Suppl. Table 1). These spikes in NO_2^-

603   (and more pronounced, NO_3^-) are likely caused by the bursting of GSOB vacuoles during

604   centrifugation (Reimers et al., 1996). GSOB mats can be associated with symbiotic anaerobic

605   ammonium-oxidizing (annamox) bacteria (Prokopenko et al., 2006). Since the annamox process

606   utilizes NO_2^- as the electron acceptor and NH_4^+ as the electron donor, a consortium of GSOB

607   mats and annamox bacteria were possible given the right conditions for proliferation in the SBB

608   depocenter. Anoxia could trigger the uptake of NO_3^- into bacterial vacuoles, creating declining

609   NO_3^- concentrations that are more favorable to DNRA in the bottom water. In these conditions,

610   GSOB in the SBB benthic environment could utilize their ability to perform DNRA to out-

611   compete similar denitrifying taxa, and proliferate into thick, contiguous mats. While low-nitrate

612   conditions could benefit GSOB mats, the mats do not persist once bottom water reaches anitria,

613   as evidenced by GSOB mat distribution during the 2013 expedition (Valentine et al., 2016).

614

615

4.3 Microbial mat proliferation and benthic phosphate remineralization dependent on high

rates of organic matter degradation in the Santa Barbara Basin

Organic carbon delivery to the benthic environment appears to be a key control on sulfate

reduction rates near the sediment-water interface as well as microbial mat proliferation. Sulfate

reduction rates in the SBB depocenter are most similar in magnitude and profile (i.e., highest

rates found at the sediment-water interface and decline drastically thereafter) to those found in

sediments below the transiently deoxygenated portion of the Peruvian shelf (e.g., 4.1 mmol m^{-2}

d^{-1} at the SBB NDRO station vs. 2.5-3.8 mmol m^{-2} d^{-1} at 128-144 m water depth on the Peruvian

margin (Gier et al., 2016; Treude et al., 2021)). The TOC content of surface sediments in these

two regions are both high and within the same order of magnitude; 5.3% in SBB depocenter

compared with 7.6% in the Peruvian margin 145 m depth (Noffke et al., 2012). In comparison,

sulfate reduction rates in the SBB were at least one order of magnitude lower than found in

sediment below the OMZ on the Namibian Shelf, which has much higher TOC contents of >10%

(Brüchert et al., 2003; Bremner, 1981). Sulfate reduction rates in the shelf sediments below the

Eastern Arabian OMZ were an order of magnitude lower (0.18 – 1.27 mmol m^{-2} d^{-1}) than rates in

the SBB depocenter (Naik et al., 2017) despite similar hypoxic to anoxic bottom water

conditions. These lower rates were attributed to the relatively low benthic organic matter

delivery compared to other transiently deoxygenated systems (surface sediment TOC content

approx. 2 – 3%) (Naik et al., 2017). Sedimentary organic matter content appears to be important

in the proliferation of GSOB mats; too much TOC could result in toxic levels of sulfide at the

sediment-water interface (*Beggiatoa* exhibit an aversion to sulfidic sediments but toxicity has not

638   been quantified, (Preisler et al., 2007)) whereas too little sulfide would not provide enough

639   electron donor for the GSOB's chemoautotrophic metabolism.

640

641   The profiles of several indicators for benthic anaerobic organic matter remineralization (total

642   alkalinity, DIC, PO_4^{3-}, NH_4^+) increased in steepness with increasing water depth (Figs. 2 A-E &

643   3A-F). One divergence from this trend can be seen in PO_4^{3-} profiles from the shallow C and D

644   stations, which also featured low rates of sulfate reduction. PO_4^{3-} profiles in these sediment track

645   closely to Fe^{2+} profiles; both solutes dip in concentration in areas with visible iron sulfide

646   formation (e.g., 5-11 cm in NDT3-D as seen in Fig. 2A). Additionally, several stations that

647   exhibited high sulfate reduction rates in surface sediment (e.g., SDT1-A) showed almost no

648   change in PO_4^{3-} at depths below 5 cm (e.g., Fig. 2 K-O compared to Fig. 2 A-E). This

649   phenomenon has been previously documented in SBB sediment and is attributed to the

650   precipitation of carbonate fluorapatite (Reimers et al., 1996). The confinement of these flat PO_4^{3-}

651   profiles to stations with >100 nmol cm^{-3} d^{-1} sulfate reduction in surface sediment suggests that

652   this mineralogical sink of PO_4^{3-} in SBB sediment may be dependent on high sulfate reduction

653   rates, owing to the bicarbonate produced by sulfate reduction (Reimers et al., 1996), and is not

654   found throughout the basin. Flat PO_4^{3-} profiles were also reported from the transiently

655   deoxygenated portion of the Peruvian OMZ, where phosphate mineral precipitation has been

656   documented (Noffke et al., 2012). Similar to the shallow margins of the SBB, PO_4^{3-} in

657   Mauritanian OMZ porewater tracks closely with changes in porewater Fe^{2+} (Schroller-Lomnitz

658   et al., 2019), indicating that iron mineralization/dissolution mechanics hold a greater influence

659   on PO_4^{3-} concentrations under hypoxic bottom waters.

660

4.3 Iron cycling dictates the location of sulfate reduction in Santa Barbara Basin sediment.

While low or absent oxygen concentrations in the bottom water appeared to facilitate sulfate

reduction close to the sediment-water interface in the SBB (e.g., NDRO and NDT3-A as seen in

fig. 2N and 2O), iron sulfide formation in deeper sediment layers may also play a crucial role in

controlling the distribution of sulfate reduction. SBB sediments showed a wide vertical and

horizontal heterogeneity of redox states based on visual appearance (Fig. 1A-K). Sediment

beneath the hypoxic bottom water at the shallowest D stations was reddish, consistent with a

high content of iron oxides. Interestingly, porewater Fe^{2+} concentrations in shallower parts of the

basin (e.g., NDT3-D, max. ~700 μM Fe^{2+}) were an order of magnitude larger than those found

anywhere in both the Peruvian (max ~60 and ~30 μM Fe^{2+}, respectively; Noffke et al., 2012;

Plass et al., 2020) and Mauritanian (max. ~50 μM Fe^{2+}; Schroller-Lomnitz et al 2019) OMZ.

Deeper in the basin, bands of black sediment that appear mid-core at NDT3-C (6-14 cm) and

SDT3-C (6-10 cm) indicate the formation of iron sulfides as a result of sulfide produced by

sulfate reduction (Canfield, 1989). At the C stations, peaks in sulfate reduction were located in

the surface sediment, above the iron sulfide layers, and declined below approx. 4 cm, indicating

a discrepancy between observed peak sulfate reduction activity and the mineralogical clues left

behind by the process.

Comparing data from shallow stations at the same depth (e.g., NDT3-C vs. SDT3-C) revealed

differences in sediment sulfate reduction in the SBB, potentially due to changes in iron

mineralogy. Both D-stations had similar bottom water conditions (Table 1), sulfate reduction

rates (Fig. 3W-AG), porewater concentrations of solutes (Figs. 2 and 3), and visual sediment

684   characteristics (Section 3.1). On the contrary, there are some noticeable differences in the

685   porewater geochemistry between the two C-stations, which in contrast to D-stations are below

686   the SBB sill depth, irrespective of similar bottom water oxygen conditions. NDT3-C porewater

687   Fe^{2+} concentration (Fig. 2G) peaked in the top 1 cm of sediment (similar to deeper stations)

688   while SDT3-C porewater Fe^{2+} concentration (Fig. 3H) peaked around 5-cm sediment depth.

689   NDT3-C sediment (Table 1B) exhibited iron sulfide formation from approx. 6-14 cm sediment

690   depth, while SDT3-C sediment (Table 1J) had a much narrower band around 8-10 cm (the same

691   depth at which Fe^{2+} concentrations decrease in the porewater). Finally, the sulfate reduction rate

692   at NDT3-C (Fig. 2L) mirrored deeper station profiles (e.g., NDRO in Fig. 2O) rather than other

693   shallow station profiles (e.g., SDT3-C in Fig. 3N). While sulfate reduction rates for B-stations

694   are absent, porewater Fe^{2+} profiles show a similar difference between the north and south basin

695   (Fig. 2H compared to Fig. 3I) as did visual sediment characteristics (Table 1C compared to 1I).

696   This difference in biogeochemical profiles and apparent minerology between the north and south

697   C and B stations could be a result of hydrographic and/or bathymetric differences in the basin

698   (Sholkovitz and Gieskes, 1971; Bograd et al., 2002), but a discernable link between the

699   differences in sediment biogeochemistry and the differences in bottom water oxygen (Table 1)

700   need to be further explored.

701

702   Deeper in the basin (depocenter and A-stations), porewater Fe^{2+} concentrations in sediment

703   beneath anoxic bottom water (max. 84 µM Fe^{2+}) were similar to concentrations found below the

704   Peruvian OMZ in 2008 under anoxic bottom water conditions (78 m water depth, max. 80 µM

705   Fe^{2+}) (Noffke et al., 2012). SBB porewater Fe^{2+} concentrations were an order of magnitude

706   larger than those found at a similar site on the Peruvian shelf (75 m water depth, max. 1 µM

707   Fe^{2+}) in 2017 during a kelvin-wave-associated "Coastal El Niño" event that created oxygenated

708   bottom waters during the sampling and the disappearance of previously observed dense GSOB

709   mats (Plass et al., 2020). As the SBB water column was undergoing rapid deoxygenation in the

710   weeks preceding this study (Qin et al., 2022), the sediments below the sill appeared to be

711   actively shifting from a ferruginous state to a sulfidic state, with this change starting around the

712   C stations and being complete in the depocenter. Comparing apparent iron sulfide formation with

713   dips in porewater Fe^{2+} concentrations in C-station profiles (Fig. 1B compared to Fig. 2G and Fig.

714   1J compared to Fig. 3H) signals a shift away from a ferruginous state occurring just below the

715   SBB sill.

716

717   C-station porewater Fe^{2+} concentrations and sulfate reduction rates indicate that migration of the

718   sulfate reduction zone towards the sediment-water interface is associated with iron sulfide

719   formation deeper in the sediment. The activity of cable bacteria, which are able to bridge the gap

720   between the oxidized sediment-water interface and reduced sediment below using a biofilament

721   (Pfeffer et al., 2012), could explain the interplay between sulfate reduction and iron cycling in

722   SBB sediments. Cable bacteria contain the genes required for DNRA (Kjeldsen et al., 2019) and

723   can perform nitrate reduction in incubation experiments (Marzocchi et al., 2014), but their direct

724   transformation of NO_3^- in the environment appears limited (Kessler et al., 2019) and they appear

725   to be inactive in anoxic aquatic environments (Seitaj et al., 2015; Marzocchi et al., 2018). Cable

726   bacteria primarily conduct aerobic sulfide oxidation (Pfeffer et al., 2012), though they can also

727   utilize Fe^{2+} as an electron donor (Seitaj et al., 2015). The maximum recorded filament length of

728   cable bacteria is 7 cm (Van De Velde et al., 2016), roughly in line with the appearance of black

729   sediment in the SBB C-station sediments. Further, cable bacteria have been found to directly

730   compete with GSOB in transiently deoxygenated systems, with cable bacteria active under

731   oxygenated conditions and GSOB active in anoxic conditions (Seitaj et al., 2015). Cable

732   bacteria can also prevent the formation of euxinic conditions at the sediment-water interface via

733   the creation of an iron-oxide buffer (formed through Fe^{2+} oxidation) in near-surface sediments

734   (Seitaj et al., 2015). Therefore, if cable bacteria activity in the SBB decreased with declining

735   oxygen concentrations below the sill, their iron oxide buffer could have been reduced,

736   encouraging the sulfate reduction zone to migrate towards the sediment surface (as seen at

737   NDT3-C). The presence of cable bacteria can be detected by a slight increase in pH below the

738   sediment-water interface (typically pH > 8) (Schauer et al., 2014), which was not reflected in our

739   pH results, but forthcoming DNA analyses from these sediments should elucidate the role cable

740   bacteria play in the SBB. Additionally, forthcoming sequential iron and sulfur extractions from

741   SBB sediments should provide more information about the differences in early diagenesis

742   throughout the basin.

743

744   **4.4 Iron and phosphate flux into SBB bottom water is a feature of transient deoxygenation.**

745

746   As postulated previously (Kuwabara et al., 1999), oxidation of iron sulfides at the sediment-

747   water interface upon basin flushing with oxygen likely encourages microbial iron reduction

748   following later deoxygenation. This iron reduction causes strong $Fe^{2+}$and PO_4^{3-} fluxes out of

749   SBB depocenter sediment. High porewater Fe^{2+} concentration (>100 µM) in the SBB D stations

750   (Figs. 3L and V) indicate regions of prolific bacterial iron reduction in the sediment. As basin

751   depth increases and oxygen concentration in the water decreases, the zone of iron reduction thins

752   and is found closer to the sediment-water interface (Figs. 2 & 3). Further, high benthic fluxes of

753   Fe^{2+} and PO_4^{3-} were observed in the transiently anoxic depocenter (Fig. 5). High Fe^{2+} and PO_4^{3-}

754   fluxes were also seen on the Peruvian shelf during transient anoxia (Noffke et al., 2012). The

755   release of these solutes was interpreted to be sourced from a layer of reactive iron hydroxides

756   existing near the sediment surface, likely established during a recent oxygenation event. Similar

757   conditions, i.e., visibly oxidized (reddish) sediment laminae and a thin zone of iron reduction

758   apparent from a peak in Fe^{2+} at the sediment-water interface, were found in sediment from the

759   SBB depocenter. These analogous observations highlight the importance of alternating redox

760   conditions to establish high benthic iron fluxes. On the contrary, the persistently anoxic core of

761   the Peruvian OMZ appears to have little to no benthic flux of Fe^{2+} and PO_4^{3-} into the bottom

762   water (Noffke et al., 2012). Here, iron at the sediment-water interface is hypothesized to be

763   locked up in iron sulfides, which are rarely re-oxidized due to persistent anoxia.

764

765   It is further notable that benthic fluxes of Fe^{2+} and PO_4^{3-} from the SBB depocenter were approx.

766   five times higher (Fig. 5) compared to the Peruvian shelf (4.9 vs. 0.9 mmol Fe^{2+} m^{-2} d^{-1} and 3.6

767   vs. 0.8 mmol PO_4^{3-} m^{-2} d^{-1}, respectively) (Noffke et al., 2012). Based on Fe^{2+} profiles, the zone of

768   iron reduction in Peruvian shelf sediments extended down to approx. 10 cm, while the zone

769   appeared to be much shallower and narrower (less than the top 5 cm) in the SBB depocenter.

770   These differences in magnitude of Fe^{2+} concentration and Fe^{2+} and PO_4^{3-} flux between the SBB

771   depocenter and the Peruvian shelf could be attributed to differences in the recency and

772   magnitude of reoxygenation events. The release of Fe^{2+} from sediment into the bottom water

773   could create a buffer against reoxygenation in transiently deoxygenated systems, giving a

774   competitive advantage to anaerobic benthic metabolisms (Dale et al., 2013; Wallmann et al.,

775   2022). Additionally, both Fe^{2+} and PO_4^{3-} release from the SBB sediment could allow for higher

776   rates of primary productivity if those constituents diffused into the photic zone (Robinson et al.,

777   2022). The fate of Fe^{2+} and PO_4^{3-} diffusing into SBB waters from the sediment-water interface is

778   a focus of ongoing work within the basin.

779
780   **5 Conclusions**
781

782   This research expands upon the wealth of science already conducted in the SBB and other

783   transiently deoxygenated environments by examining changes in benthic biogeochemistry

784   promoted by the onset of anoxia. We found that GSOB mats proliferate in the SBB where the

785   bottom water is anoxic and nitrate concentrations are declining, initiating a shift from primarily

786   denitrification to an increase in DNRA. We conclude that GSOB mat proliferation in the SBB is

787   confined to areas of the benthic environment with anoxic (though not completely anitric) bottom

788   water. The sulfate reduction zone is elevated to the surface sediments underneath theses mats,

789   but mat presence alone seems insufficient to change the depth of sulfate reduction. We conclude

790   that changes in iron minerology, specifically the formation of an iron sulfide layer deeper in

791   sediments, encourages the elevation of the sulfate reduction zone. If anoxic events become

792   longer and more frequent in the SBB because of global warming (Qin et al., 2022; Stramma et

793   al., 2008), the iron oxide buffer built up in shallower depths (e.g., NDT3-B) could be exhausted,

794   allowing for surface sulfate reduction and the proliferation of GSOB mats in shallower margins

795   of the basin than currently seen. Further, the same transient deoxygenation that allows for these

796   mats to flourish also allows for a high Fe^{2+} and PO_4^{3-} flux into the SBB water column. In order to

797   fully understand the complex changes in the benthic environment in response to deoxygenation,

798   genomic and molecular work of the upper sediment community needs to be characterized.

799   Overall, the insights gleaned from this research will aid in the understanding of fundamental

800   biogeochemical changes that occur when marine environments become anoxic.

801   **Acknowledgements**

802   We thank the captain, crew, and scientific party of the R/V Atlantis, and the crew of the ROV

803   Jason for their technical and logistical support during the research expedition AT42-19. We also

804   thank Q. Qin, E. Arrington, M. O'Beirne, A. Mazariegos, X. Moreno, A. Eastman, and K.

805   Gosselin for assisting with shipboard analyses. We further thank M. Alisch from the Max-

806   Planck-Institute in Bremen, Germany for DIC analyses. We thank G. Eickert-Grötzschel, V.

807   Hübner, A. Niclas, I. Schröder, and C. Wigand from the Max-Planck-Institute in Bremen,

808   Germany for constructing the microsensors. We acknowledge J. Matthews from the UC Davis

809   Stable Isotope facility for assisting with solid phase analyses. Funding for this work was

810   provided by the US National Science Foundation, NSF OCE-1756947 and OCE-1830033 (to

811   DLV) and OCE-1829981 (to TT). Further support was provided by the Max Planck Society and

812   the Alfred Wegener Institute for Polar and Marine Research.

813

814   **Data availability.**

815   Biogeochemical data presented in this manuscript are accessible through the Biological &

816   Chemical Oceanography Data Management Office (BCO-DMO) at the following landing pages:

817   https://www.bco-dmo.org/dataset/867007; https://www.bco-dmo.org/dataset/867113;

818   https://www.bco-dmo.org/dataset/867221; https://www.bco-dmo.org/dataset/896706

Author contributions.

TT, DV, FK, NL, and JT designed the project. DJY, SK, JT, DR, and TT processed sediment

cores at sea. DJY conducted geochemical analyses of sediment porewater and benthic flux

chamber water. DJY prepared TOC and TON samples. DR and SK analyzed sediment porosity

and density. TT and SK performed shipboard sulfate reduction incubations. DJY and DR

conducted sulfate reduction analyses. DJY, NL, and JT transformed and interpreted ROV Jason

data. FJ and FW operated BFC and microprofilers and analyzed associated data. XP conducted

^{15}N experiments and analyses.

Competing interests.

At least one of the (co-)authors is a member of the editorial board of Biogeosciences.

830   **References**
831
832   Bernhard, J. M., Visscher, P. T., and Bowser, S. S.: Submillimeter life positions of bacteria,
833   protists, and metazoans in laminated sediments of the Santa Barbara Basin, Limnology
834   and Oceanography, 48, 813-828, 2003.
835   Bograd, S. J., Schwing, F. B., Castro, C. G., and Timothy, D. A.: Bottom water renewal in the
836   Santa Barbara Basin, Journal of Geophysical Research: Oceans, 107, 9-1-9-9, 2002.
837   Bourbonnais, A., Letscher, R. T., Bange, H. W., Echevin, V., Larkum, J., Mohn, J., Yoshida, N., and
838   Altabet, M. A.: N2O production and consumption from stable isotopic and concentration
839   data in the Peruvian coastal upwelling system, Global Biogeochemical Cycles, 31, 678-
840   698, 2017.
841   Bremner, J.: Biogenic sediments on the South West African continental margin, 1981.
842   Brüchert, V., Jørgensen, B. B., Neumann, K., Riechmann, D., Schlösser, M., and Schulz, H.:
843   Regulation of bacterial sulfate reduction and hydrogen sulfide fluxes in the central
844   Namibian coastal upwelling zone, Geochim. Cosmochim. Acta, 67, 4505-4518, 2003.
845   California Cooperative Oceanic Fisheries Investigations: https://www.calcofi.org/ccdata.html,
846   last
847   Canfield, D. E.: Reactive iron in marine sediments, Geochimica et cosmochimica acta, 53, 619-
848   632, 1989.
849   Canfield, D. E., Stewart, F. J., Thamdrup, B., De Brabandere, L., Dalsgaard, T., Delong, E. F.,
850   Revsbech, N. P., and Ulloa, O.: A cryptic sulfur cycle in oxygen-minimum–zone waters off
851   the Chilean coast, Science, 330, 1375-1378, 2010.
852   Charoenpong, C. N., Bristow, L. A., and Altabet, M. A.: A continuous flow isotope ratio mass
853   spectrometry method for high precision determination of dissolved gas ratios and
854   isotopic composition, Limnology and Oceanography: Methods, 12, 323-337, 2014.
855   Cline, J. D.: Spectrophometric determination of hydrogen sulfide in natural waters, Limnol.
856   Oceanogr., 14, 454-458, 1969.
857   Dale, A. W., Bertics, V. J., Treude, T., and Wallmann, K.: Modeling benthic-pelagic nutrient
858   exchange processes and porewater distributions in a seasonally hypoxic sediment:
859   evidence for massive phosphate release by Beggiatoa?, Biogeosciences, 10, 629-651,
860   2013.
861   Dale, A. W., Sommer, S., Lomnitz, U., Bourbonnais, A., and Wallmann, K.: Biological nitrate
862   transport in sediments on the Peruvian margin mitigates benthic sulfide emissions and
863   drives pelagic N loss during stagnation events, Deep Sea Research Part I: Oceanographic
864   Research Papers, 112, 123-136, 2016.
865   Dale, A. W., Sommer, S., Ryabenko, E., Noffke, A., Bohlen, L., Wallmann, K., Stolpovsky, K.,
866   Greinert, J., and Pfannkuche, O.: Benthic nitrogen fluxes and fractionation of nitrate in
867   the Mauritanian oxygen minimum zone (Eastern Tropical North Atlantic), Geochimica et
868   Cosmochimica Acta, 134, 234-256, 2014.
869   Dale, A. W., Sommer, S., Bohlen, L., Treude, T., Bertics, V. J., Bange, H. W., Pfannkuche, O.,
870   Schorp, T., Mattsdotter, M., and Wallmann, K.: Rates and regulation of nitrogen cycling
871   in seasonally hypoxic sediments during winter (Boknis Eck, SW Baltic Sea): Sensitivity to
872   environmental variables, Estuar. Continent. Shelf Sci., 95, 14-28, 2011.

873   Dale, A. W., Sommer, S., Lomnitz, U., Montes, I., Treude, T., Liebetrau, V., Gier, J., Hensen, C.,
874   Dengler, M., Stolpovsky, K., Bryant, L. D., and Wallmann, K.: Organic carbon production,
875   mineralisation and preservation on the Peruvian margin, Biogeosciences, 12, 1537-1559,
876   2015.
877   Emery, K., Hülsemann, J., and Rodolfo, K.: Influence of turbidity currents upon basin waters,
878   Limnology and Oceanography, 7, 439-446, 1962.
879   Emmer, E. and Thunell, R. C.: Nitrogen isotope variations in Santa Barbara Basin sediments:
880   Implications for denitrification in the eastern tropical North Pacific during the last
881   50,000 years, Paleoceanography, 15, 377-387, 2000.
882   Fossing, H., Gallardo, V. A., Jørgensen, B. B., Hüttel, M., Nielsen, L. P., Schulz, H., Canfield, D. E.,
883   Forster, S., Glud, R. N., and Gundersen, J. K.: Concentration and transport of nitrate by
884   the mat-forming sulphur bacterium Thioploca, Nature, 374, 713-715, 1995a.
885   Fossing, H., Gallardo, V. A., Jørgensen, B. B., Hüttel, M., Nielsen, L. P., Schulz, H., Canfield, D. E.,
886   Forster, S., Glud, R. N., Gundersen, J. K., Küver, J., Ramsing, N. B., Teske, A., Thamdrup,
887   B., and Ulloa, O.: Concentration and transport of nitrate by the mat-forming sulphur
888   bacterium Thioploca, Nature, 374, 713-715, 1995b.
889   García-Robledo, E., Corzo, A., and Papaspyrou, S.: A fast and direct spectrophotometric method
890   for the sequential determination of nitrate and nitrite at low concentrations in small
891   volumes, Marine Chemistry, 162, 30-36, 2014.
892   Gier, J., Sommer, S., Löscher, C. R., Dale, A. W., Schmitz, R. A., and Treude, T.: Nitrogen fixation
893   in sediments along a depth transect through the Peruvian oxygen minimum zone,
894   Biogeosciences, 13, 4065–4080, 2016.
895   Glud, R. N., Gundersen, J. K., and Ramsing, N. B.: Electrochemical and optical oxygen
896   microsensors for in situ measurements, in: In situ monitoring of aquatic systems:
897   Chemical analysis and speciation, edited by: Buffle, J., and Horvai, G., Wiley, 2000.
898   Goericke, R., Bograd, S. J., and Grundle, D. S.: Denitrification and flushing of the Santa Barbara
899   Basin bottom waters, Deep Sea Research Part II: Topical Studies in Oceanography, 112,
900   53-60, 2015.
901   Grasshoff, K., Ehrhardt, M., and Kremling, K.: Methods of seawater analysis, Wiley-VCH Verlag
902   GmbH, Weinheim1999.
903   Gundersen, J. K. and Jørgensen, B. B.: Microstructure of diffusive boundary layers and the
904   oxygen uptake of the sea floor, Nature, 345, 604-607, 1990.
905   Hall, P. O. J. and Aller, R. C.: Rapid small-volume flow injection analysis for $\sum CO_2$ and NH_4^+ in
906   marine and fresh waters, Limnol. Oceanogr., 37, 1113-1119, 1992.
907   Harris, D., Horwáth, W. R., and Van Kessel, C.: Acid fumigation of soils to remove carbonates
908   prior to total organic carbon or carbon‑13 isotopic analysis, Soil Science Society of
909   America Journal, 65, 1853-1856, 2001.
910   Hossain, M., Bhattacharya, P., Frape, S. K., Jacks, G., Islam, M. M., Rahman, M. M., von
911   Brömssen, M., Hasan, M. A., and Ahmed, K. M.: Sediment color tool for targeting
912   arsenic-safe aquifers for the installation of shallow drinking water tubewells, Science of
913   the Total Environment, 493, 615-625, 2014.

914   Huettel, M., Forster, S., Kloser, S., and Fossing, H.: Vertical migration in the sediment-dwelling
915   sulfur bacteria Thioploca spp. in overcoming diffusion limitations, Applied and
916   Environmental Microbiology, 62, 1863-1872, 1996.
917   Høgslund, S., Revsbech, N. P., Kuenen, J. G., Jørgensen, B. B., Gallardo, V. A., Vossenberg, J. v.
918   d., Nielsen, J. L., Holmkvist, L., Arning, E. T., and Nielsen, L. P.: Physiology and behaviour
919   of marine Thioploca, The ISME journal, 3, 647-657, 2009.
920   Jensen, M. M., Lam, P., Revsbech, N. P., Nagel, B., Gaye, B., Jetten, M. S., and Kuypers, M. M.:
921   Intensive nitrogen loss over the Omani Shelf due to anammox coupled with dissimilatory
922   nitrite reduction to ammonium, The ISME journal, 5, 1660-1670, 2011.
923   Jeroschewsky, P., Steuckart, C., and Kuehl, M.: An amperometric microsensor for the
924   determination af H2S in aquatic environments, Anal. Chem., 68, 4351-4357, 1996.
925   Jørgensen, B.: Distribution of colorless sulfur bacteria (Beggiatoa spp.) in a coastal marine
926   sediment, Marine Biology, 41, 19-28, 1977.
927   Jørgensen, B. B.: A comparison of methods for the quantification of bacterial sulphate reduction
928   in coastal marine sediments: I. Measurements with radiotracer techniques,
929   Geomicrobiol. J., 1, 11-27, 1978.
930   Jørgensen, B. B. and Nelson, D. C.: Sulfide oxidation in marine sediments: Geochemistry meets
931   microbiology, Geological Society of America, Special Paper 379, 63-81, 2004.
932   Kallmeyer, J., Ferdelman, T. G., Weber, A., Fossing, H., and Jørgensen, B. B.: A cold chromium
933   distillation procedure for radiolabeled sulfide applied to sulfate reduction
934   measurements, Limnol. Oceanogr. Methods, 2, 171-180, 2004.
935   Kessler, A. J., Wawryk, M., Marzocchi, U., Roberts, K. L., Wong, W. W., Risgaard‐Petersen, N.,
936   Meysman, F. J., Glud, R. N., and Cook, P. L.: Cable bacteria promote DNRA through iron
937   sulfide dissolution, Limnology and Oceanography, 64, 1228-1238, 2019.
938   Kjeldsen, K. U., Schreiber, L., Thorup, C. A., Boesen, T., Bjerg, J. T., Yang, T., Dueholm, M. S.,
939   Larsen, S., Risgaard-Petersen, N., and Nierychlo, M.: On the evolution and physiology of
940   cable bacteria, Proceedings of the National Academy of Sciences, 116, 19116-19125,
941   2019.
942   Kononets, M., Tengberg, A., Nilsson, M., Ekeroth, N., Hylén, A., Robertson, E. K., Van De Velde,
943   S., Bonaglia, S., Rütting, T., and Blomqvist, S.: In situ incubations with the Gothenburg
944   benthic chamber landers: Applications and quality control, Journal of Marine Systems,
945   214, 103475, 2021.
946   Kuwabara, J. S., van Geen, A., McCorkle, D. C., and Bernhard, J. M.: Dissolved sulfide
947   distributions in the water column and sediment pore waters of the Santa Barbara Basin,
948   Geochimica et Cosmochimica Acta, 63, 2199-2209, 1999.
949   Levin, L. A., Gutierrez, D., Rathburn, A. E., Neira, C., Sellanes, J., Munoz, P., Gallardo, V. A., and
950   Salamance, M.: Bethic processes on the Peru margin: a transect across the oxygen
951   minimum zone during the 1997-98 El Nino, Prog. Oceanog., 53, 1-27, 2002.
952   Marchant, H. K., Lavik, G., Holtappels, M., and Kuypers, M. M.: The fate of nitrate in intertidal
953   permeable sediments, PloS one, 9, e104517, 2014.
954   Marzocchi, U., Bonaglia, S., van de Velde, S., Hall, P. O., Schramm, A., Risgaard‐Petersen, N.,
955   and Meysman, F. J.: Transient bottom water oxygenation creates a niche for cable

956 bacteria in long-term anoxic sediments of the Eastern Gotland Basin, Environmental
957   microbiology, 20, 3031-3041, 2018.
958 Marzocchi, U., Trojan, D., Larsen, S., Louise Meyer, R., Peter Revsbech, N., Schramm, A., Peter
959   Nielsen, L., and Risgaard-Petersen, N.: Electric coupling between distant nitrate
960   reduction and sulfide oxidation in marine sediment, The ISME journal, 8, 1682-1690,
961   2014.
962 Middelburg, J. and Levin, L.: Coastal hypoxia and sediment biogeochemistry, Biogeosciences, 6,
963   1273-1293, 2009.
964 Mosch, T., Sommer, S., Dengler, M., Noffke, A., Bohlen, L., Pfannkuche, O., Liebetrau, V., and
965   Wallmann, K.: Factors influencing the distribution of epibenthic megafauna across the
966   Peruvian oxygen minimum zone, Deep Sea Research Part I: Oceanographic Research
967   Papers, 68, 123-135, 2012.
968 Mußmann, M., Schulz, H. N., Strotmann, B., Kjær, T., Nielsen, L. P., Rosselló-Mora, R. A.,
969   Amann, R. I., and Jørgensen, B. B.: Phylogeny and distribution of nitrate-storing
970   Beggiatoa spp. in coastal marine sediments, Environmental Microbiology, 5, 523-533,
971   2003.
972 Naik, R., Naqvi, S., and Araujo, J.: Anaerobic carbon mineralisation through sulphate reduction
973   in the inner shelf sediments of eastern Arabian Sea, Estuaries and Coasts, 40, 134-144,
974   2017.
975 Noffke, A., Hensen, C., Sommer, S., Scholz, F., Bohlen, L., Mosch, T., Graco, M., and Wallmann,
976   K.: Benthic iron and phosphorus fluxes across the Peruvian oxygen minimum zone,
977   Limnol. Oceanogr., 57, 851-867, 2012.
978 Pavlova, G. Y., Tishchenko, P. Y., Volkova, T., Dickson, A., and Wallmann, K.: Intercalibration of
979   Bruevich's method to determine the total alkalinity in seawater, Oceanology, 48, 438-
980   443, 2008.
981 Peng, X., Ji, Q., Angell, J. H., Kearns, P. J., Yang, H. J., Bowen, J. L., and Ward, B. B.: Long-term
982   fertilization alters the relative importance of nitrate reduction pathways in salt marsh
983   sediments, Journal of Geophysical Research: Biogeosciences, 121, 2082-2095, 2016.
984 Pfeffer, C., Larsen, S., Song, J., Dong, M., Besenbacher, F., Meyer, R. L., Kjeldsen, K. U.,
985   Schreiber, L., Gorby, Y. A., and El-Naggar, M. Y.: Filamentous bacteria transport
986   electrons over centimetre distances, Nature, 491, 218-221, 2012.
987 Plass, A., Schlosser, C., Sommer, S., Dale, A. W., Achterberg, E. P., and Scholz, F.: The control of
988   hydrogen sulfide on benthic iron and cadmium fluxes in the oxygen minimum zone off
989   Peru, Biogeosciences, 17, 3685-3704, 2020.
990 Preisler, A., De Beer, D., Lichtschlag, A., Lavik, G., Boetius, A., and Jørgensen, B. B.: Biological
991   and chemical sulfide oxidation in a Beggiatoa inhabited marine sediment, ISME Journal,
992   341-351, 2007.
993 Prokopenko, M., Hammond, D., Berelson, W., Bernhard, J., Stott, L., and Douglas, R.: Nitrogen
994   cycling in the sediments of Santa Barbara basin and Eastern Subtropical North Pacific:
995   Nitrogen isotopes, diagenesis and possible chemosymbiosis between two lithotrophs
996   (Thioploca and Anammox)—"riding on a glider", Earth and Planetary Science Letters,
997   242, 186-204, 2006.

998 Qin, Q., Kinnaman, F. S., Gosselin, K. M., Liu, N., Treude, T., and Valentine, D. L.: Seasonality of
999   Water Column Methane Oxidation and Deoxygenation in a Dynamic Marine
1000   Environment, Geochimica et Cosmochimica Acta, 2022.
1001 Reimers, C. E., Ruttenberg, K. C., Canfield, D. E., Christiansen, M. B., and Martin, J. B.: Porewater
1002   pH and authigenic phases formed in the uppermost sediments of Santa Barbara Basin,
1003   Geochim. Cosmochim. Acta, 60, 4037-4057, 1996.
1004 Revsbech, N. P. and Jørgensen, B. B.: Microelectrodes: their use in microbial ecology, in: Adv.
1005   Microb. Ecol., edited by: Marshall, K. C., Plenum, New York, 293-352, 1986.
1006 Robinson, D. M., Pham, A. L., Yousavich, D. J., Janssen, F., Wenzhöfer, F., Arrington, E. C.,
1007   Gosselin, K. M., Sandoval-Belmar, M., Mar, M., and Valentine, D. L.: Iron "Ore" Nothing:
1008   Benthic iron fluxes from the oxygen-deficient Santa Barbara Basin enhance
1009   phytoplankton productivity in surface waters, Biogeosciences Discussions, 1-36, 2022.
1010 Sayama, M.: Presence of nitrate-accumulating sulfur bacteria and their influence on nitrogen
1011   cycling in a shallow coastal marine sediment, Applied and Environmental Microbiology,
1012   67, 3481-3487, 2001.
1013 Schauer, R., Risgaard-Petersen, N., Kjeldsen, K. U., Tataru Bjerg, J. J., B Jørgensen, B., Schramm,
1014   A., and Nielsen, L. P.: Succession of cable bacteria and electric currents in marine
1015   sediment, The ISME journal, 8, 1314-1322, 2014.
1016 Schroller-Lomnitz, U., Hensen, C., Dale, A. W., Scholz, F., Clemens, D., Sommer, S., Noffke, A.,
1017   and Wallmann, K.: Dissolved benthic phosphate, iron and carbon fluxes in the
1018   Mauritanian upwelling system and implications for ongoing deoxygenation, Deep Sea
1019   Research Part I: Oceanographic Research Papers, 143, 70-84, 2019.
1020 Schulz, H. N. and Schulz, H. D.: Large sulfur bacteria and the formation of phosphorite, Science,
1021   307, 416-418, 2005.
1022 Schulz, H. N., Jorgensen, B. B., Fossing, H. A., and Ramsing, N. B.: Community structure of
1023   filamentous, sheath-building sulfur bacteria, Thioploca spp., off the coast of Chile,
1024   Applied and Environmental Microbiology, 62, 1855-1862, 1996.
1025 Schulz, H. N., Brinkhoff, T., Ferdelman, T. G., Hernández Mariné, M., Teske, A., and Jørgensen,
1026   B. B.: Dense populations of a giant sulfur bacterium in Namibian shelf sediments,
1027   Science, 284, 493-495, 1999.
1028 Seitaj, D., Schauer, R., Sulu-Gambari, F., Hidalgo-Martinez, S., Malkin, S. Y., Burdorf, L. D.,
1029   Slomp, C. P., and Meysman, F. J.: Cable bacteria generate a firewall against euxinia in
1030   seasonally hypoxic basins, Proceedings of the National Academy of Sciences, 112,
1031   13278-13283, 2015.
1032 Sholkovitz, E.: Interstitial water chemistry of the Santa Barbara Basin sediments, Geochimica et
1033   Cosmochimica Acta, 37, 2043-2073, 1973.
1034 Sholkovitz, E. R. and Gieskes, J. M.: A PHYSICAL–CHEMICAL STUDY OF THE FLUSHING OF THE
1035   SANTA BARBARA BASIN 1, Limnology and Oceanography, 16, 479-489, 1971.
1036 Sigman, D. M., Robinson, R., Knapp, A., Van Geen, A., McCorkle, D., Brandes, J., and Thunell, R.:
1037   Distinguishing between water column and sedimentary denitrification in the Santa
1038   Barbara Basin using the stable isotopes of nitrate, Geochemistry, Geophysics,
1039   Geosystems, 4, 2003.

1040   Sommer, S., Gier, J., Treude, T., Lomnitz, U., Dengler, M., Cardich, J., and Dale, A. W.: Depletion
1041   of oxygen, nitrate and nitrite in the Peruvian oxygen minimum zone cause an imbalance
1042   of benthic nitrogen fluxes, Deep-Sea Res. I, 112, 113–122, 2016.
1043   Stramma, L., Johnson, G. C., Sprintall, J., and Mohrholz, V.: Expanding oxygen-minimum zones in
1044   the tropical oceans, Science, 320, 655-658, 2008.
1045   Sverdrup, H. and Allen, W.: Distribution of diatoms in relation to the character of water masses
1046   and currents off Southern California in 1938, J. mar. Res, 2, 131-144, 1939.
1047   Thunell, R. C.: Particle fluxes in a coastal upwelling zone: sediment trap results from Santa
1048   Barbara Basin, California, Deep Sea Research Part II: Topical Studies in Oceanography,
1049   45, 1863-1884, 1998.
1050   Treude, T.: Biogeochemical reactions in marine sediments underlying anoxic water bodies, in:
1051   Anoxia: Paleontological Strategies and Evidence for Eukaryote Survival, edited by:
1052   Altenbach, A., Bernhard, J., and Seckbach, J., Cellular Origins, Life in Extreme Habitats
1053   and Astrobiology (COLE) Book Series, Springer, Dordrecht, 18-38, 2011.
1054   Treude, T., Hamdan, L. J., Lemieux, S., Dale, A. W., and Sommer, S.: Rapid sulfur cycling in
1055   sediments from the Peruvian oxygen minimum zone featuring simultaneous sulfate
1056   reduction and sulfide oxidation, Limnology and Oceanography, 66, 2661-2671, 2021.
1057   Treude, T., Smith, C. R., Wenzhoefer, F., Carney, E., Bernardino, A. F., Hannides, A. K., Krueger,
1058   M., and Boetius, A.: Biogeochemistry of a deep-sea whale fall: sulfate reduction, sulfide
1059   efflux and methanogenesis, Mar. Ecol. Prog. Ser., 382, 1-21, 2009.
1060   Valentine, D. L., Fisher, G. B., Pizarro, O., Kaiser, C. L., Yoerger, D., Breier, J. A., and Tarn, J.:
1061   Autonomous marine robotic technology reveals an expansive benthic bacterial
1062   community relevant to regional nitrogen biogeochemistry, Environmental science &
1063   technology, 50, 11057-11065, 2016.
1064   Van De Velde, S., Lesven, L., Burdorf, L. D., Hidalgo-Martinez, S., Geelhoed, J. S., Van Rijswijk, P.,
1065   Gao, Y., and Meysman, F. J.: The impact of electrogenic sulfur oxidation on the
1066   biogeochemistry of coastal sediments: A field study, Geochimica et Cosmochimica Acta,
1067   194, 211-232, 2016.
1068   Wallmann, K., José, Y. S., Hopwood, M. J., Somes, C. J., Dale, A. W., Scholz, F., Achterberg, E. P.,
1069   and Oschlies, A.: Biogeochemical feedbacks may amplify ongoing and future ocean
1070   deoxygenation: a case study from the Peruvian oxygen minimum zone,
1071   Biogeochemistry, 159, 45-67, 2022.
1072   Ward, B., Devol, A., Rich, J., Chang, B., Bulow, S., Naik, H., Pratihary, A., and Jayakumar, A.:
1073   Denitrification as the dominant nitrogen loss process in the Arabian Sea, Nature, 461,
1074   78-81, 2009.
1075   Zhang, L., Altabet, M. A., Wu, T., and Hadas, O.: Sensitive measurement of NH4+ 15N/14N
1076   (δ15NH4+) at natural abundance levels in fresh and saltwaters, Analytical Chemistry, 79,
1077   5297-5303, 2007.
1078   Zopfi, J., Kjær, T., Nielsen, L. P., and Jørgensen, B. B.: Ecology of Thioploca spp.: nitrate and
1079   sulfur storage in relation to chemical microgradients and influence of Thioploca spp. on
1080   the sedimentary nitrogen cycle, Applied and Environmental Microbiology, 67, 5530-
1081   5537, 2001.
1082
1083